

I.7

Principles of Near-Field Microwave Microscopy

STEVEN M. ANLAGE, VLADIMIR V. TALANOV,
AND ANDREW R. SCHWARTZ

Near-field microwave microscopy is concerned with quantitative measurement of the microwave electrodynamic response of materials on length scales far shorter than the free-space wavelength of the radiation. Here we review the basic concepts of near-field interactions between a source and sample, present an historical introduction to work in the field, and discuss a novel quantitative modeling approach to interpreting near-field microwave images. We discuss the spatial resolution and a number of concrete applications of near-field microwave microscopy to materials property measurements, as well as future prospects for new types of microscopy.

1 Introduction

Much of our understanding of materials comes from studying the interaction of electromagnetic fields with matter. The optical properties of metals, semiconductors, and dielectrics have revealed many aspects of charge and lattice dynamics in condensed matter and the study of materials at lower frequencies has also been a fruitful area of investigation [1]. For example, early evidence for a gap in the spectroscopic properties of superconductors came from microwave transmission experiments. Evidence for case-II coherence effects was also seen in measurements of the complex conductivity of superconductors [2]. The study of magnetization dynamics in ferromagnets came through measurements of ferromagnetic resonance and anti-resonance at microwave frequencies [3–5].

One thing that all of these techniques have in common is that they are carried out with measurement systems that are on the scale of the free-space wavelength of the radiation employed. For example, transmission experiments are done in the far-field of a source, and they typically require a sample on the scale of the wavelength in size. Many other experiments are carried out in resonant cavities, which are on the order of the wavelength in at least one dimension. One result is that the electrodynamic properties of the sample are averaged over macroscopic length scales. The properties of the material may in fact be varying on much shorter length scales, even into the nanometer range. Hence to measure the intrinsic response, such traditional measurements require remarkably large, pure, and homogeneous

samples to study. Most materials of interest today are complex multi-component compounds or nanoscale composites and can rarely be made homogeneous on the millimeter- or centimeter-length scales required for traditional electrodynamics measurements. In addition, the typical dimensions of devices into which some of these functional materials are integrated are orders of magnitude smaller than the wavelength at the frequency of operation of the device.

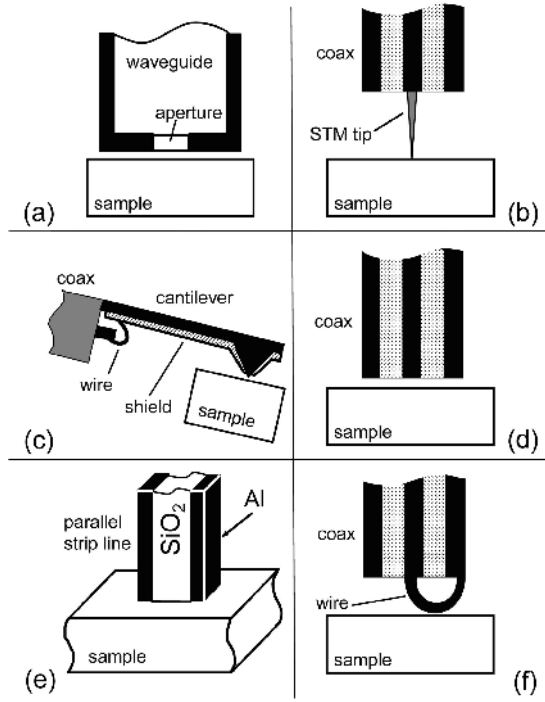
Additional constraints of traditional measurements are imposed by the sample geometry. Ideally, one would like to measure the properties of ellipsoidally shaped samples to eliminate de-magnetization and de-polarization effects, but such samples are rarely available, particularly for novel and interesting materials. Thin-film samples often have such large de-magnetization factors that results of measurements in perpendicular fields are extremely challenging to interpret, particularly on anisotropic materials. A related issue concerns the edges and corners of superconductors in the Meissner state, at which screening currents are known to become singular [6]. These extraordinarily large current densities result in an extreme type of weighted average of the sample properties. The properties of edges and corners, which may not be representative of the bulk, will dominate such measurements. This is an issue for single crystal, ceramic and thin-film samples.

A new paradigm of electrodynamics measurements in condensed matter physics has emerged in recent years. This is associated with the concept of so-called *near-field* interactions between a source and a sample in which near-zone fields and/or evanescent waves with high spatial frequency are created and interact with the sample. The recovery of these signals gives insight into the localized electrodynamic properties of the sample. The art of near-field microwave microscopy of materials is one aspect of this new paradigm. We are motivated in part by the deficiencies of traditional far-field measurements, as outlined above. We are also motivated by the desire to examine new physics on nanometer-length scales present in highly correlated electron systems and biological systems, as well as technologically motivated investigations of semiconductor and other functional materials on the nanometer scale.

In this review we arbitrarily confine ourselves to situations where the following four conditions are simultaneously met: (1) measurements are performed at frequencies between 100 MHz and 100 GHz (this ranges from the bottom of A-band to the top of M-band in the EU/NATO spectrum or I-band to W-band in the IEEE US electronic warfare spectrum); (2) measurements of material properties are performed; (3) there is scanning of the probe relative to the sample; and (4) the spatial resolution of the measurement is substantially ($\leq 10^{-1}$) less than the free-space wavelength. Even with such stringent constraints, there is a great deal of interesting work to discuss.

Although we have attempted to be comprehensive in our coverage of this field, it is inevitable that important work has been accidentally overlooked. We apologize to the reader in advance for these oversights. Some other review articles on microwave near-field imaging that are of possible interest to the reader include references [7–9]. We do not consider localized microwave electromagnetic field probing in this review, as the reader can find coverage of this topic in [7] and [9] and in the

FIGURE 1. The main types of near-field microwave probes: (a) aperture in a waveguide, (b) STM tip [12], (c) AFM tip [13], (d) open end of coaxial line [14], (e) parallel strip transmission line [15], (f) magnetic loop [16].



chapter by Paulson and van der Weide in this book. We also do not consider the use of scanned near-field microwave probes for nondestructive testing of structural materials, as the reader can find coverage of this in [10] and [11].

1.1 What is the “Near-Field”?

Most near-field microwave microscopes consist of a sub-wavelength antenna-like feature, i.e., the microscope’s *tip*, which is scanned in close proximity to a sample. The tip can be formed by an aperture in an opaque screen (Figure 1(a)), an electric wire formed by a sharpened rod or scanning tunneling microscopy (STM) tip (Figure 1(b)), an atomic force microscopy (AFM) tip (Figure 1(c)), an electrically open flush end of a transmission line (Figures 1d, 1e), a magnetic loop (Figure 1(f)), or a variety of other geometries. It is typically attached to some type of microwave detection apparatus such as an LC-oscillator, transmission line resonator, waveguide, etc. One monitors the electromagnetic response of the detection system as the tip is scanned over the sample either in contact or at a separation h typically much less than the tip characteristic length-scale D , in order to maintain a reasonable signal from the sample.

The study of *small* antennas, in which the size D is small compared to the wavelength of the radiation λ , naturally breaks into three categories: near-zone (static), intermediate-zone (induction), and far-zone (radiation) properties [17].

The antenna properties in the far zone (defined as $D \ll \lambda \ll r$, where r is the radius vector), are governed by the outgoing propagating waves with wavenumber $k_0 = \omega/c$, where ω is the angular frequency of the source and c is the speed of light in vacuum. The ratio of the electric and magnetic field magnitudes is $|E|/|H| = Z_v$, where Z_v is the vacuum impedance ($Z_v = 120\pi \Omega$), the fields are in-phase, transverse to the radius vector r , and fall off as $1/r$.

In the near zone of an antenna, the structure of electric and magnetic fields is more complicated, however. They have a static character while oscillating harmonically as $\exp(i\omega t)$ and their distribution strongly depends on the antenna geometry as well as electrodynamic properties of the surrounding region. The ratio $|E|/|H|$ could be much less or much greater than Z_v , the fields are not transverse and more nearly in quadrature, and they fall off as $1/r^2$ or faster, depending on the multipole order of the antenna. Retardation effects are minimal, simplifying the equations governing the fields. It has to be pointed out that in conventional antenna theory the near zone is typically defined as $D \ll r \ll \lambda$ [17], while we are interested in investigation of the *near-fields* occupying the range $D \leq r \ll \lambda$. Theoretically, by increasing the multipole order of the antenna system its near-zone field can be more strongly confined and the far field radiation reduced as much as desired [18,19].

Near-fields with purely exponential dependence on r (not due to dissipation) are often called *evanescent*. They are created as a result of scattering of electromagnetic radiation in geometries such as a cutoff waveguide [20], total internal reflection (which is employed in near-field optical microscopy), a sub-wavelength aperture in an opaque screen (can be used for near-field microwave microscopy) [21], or a lens with negative index of refraction [22]. These waves with imaginary wavenumbers do not carry energy away [17,23] and instead decay exponentially on a length-scale $\sim 1/D$ [8], where D is the characteristic size of the scatterer (e.g., sharp tip or aperture).

Fundamentally, the electrodynamic response of a near-field microwave probe is due to the ~~property~~ of either near-zone or evanescent fields to store *reactive* energy, electric and/or magnetic, in the vicinity of the microscope's tip (see Sec. 4.1 below). When a dielectric or permeable sample is brought in close proximity to the tip this energy changes, which in turn affects the electromagnetic response of the microscope's detection system.

In order to create a true near-zone or evanescent field *in the sample*, the tip characteristic size D must be small enough not only compared to the free-space wavelength λ , but also to provide $|k_s|D \ll 1$, where $k_s = \omega(\epsilon_0\epsilon_s\mu_0\mu_s)^{1/2}$ is the complex wave number of the material under test (see also [8]). In this case the tip-sample interaction can be viewed as a "cloud" of the probing electric or magnetic field penetrating the sample. The size of this cloud is on the order of the tip size D due to the static character of the near-field. Therefore the microscope spatial resolution—both lateral and in-depth—is mostly governed by the tip geometry rather than the electrodynamic properties of the sample, as will be illustrated in Sec. 4.7 through numerical simulations. However, the spatial resolution can be a function of the sample properties too as the electric fields between a sharp

AFM- or STM-like tip and a *high* permittivity sample are enhanced due to the field concentration just below the apex [8].

1.2 What Can Be Learned at Microwave Frequencies?

As mentioned above, quantitative microwave measurements have been very fruitful in the investigation of condensed matter systems. Because these measurements are so highly refined and precise, one would like to develop new experimental techniques to make them on deep sub-wavelength length scales. Optical radiation interacts with materials through quantum interactions, plasmon excitation, lattice dynamics, etc., and these interactions are strongly wavenumber dependent. As a result, it is often difficult to obtain quantitative information about optical properties of materials from near-field interactions. On the other hand, microwave frequency radiation interacts with matter in a much more straightforward classical manner. In this review we are primarily interested in quantitative imaging of materials properties, such as conductivity, dielectric constant, polarization, etc. We believe that the relative simplicity of the detected signal interpretation is one of the most important advantages of near-field microwave microscopy, and enables many new types of quantitative investigations of local physics in condensed matter systems.

2 General Principles of Microwave Microscope Design

As mentioned above, a microwave microscope consists of a scanned near-field antenna structure that is monitored by a detection system. In general, the detection system can be resonant, non-resonant or self-oscillating. The near-field antenna structure can be aperture-based or apertureless (Figure 1). In the latter case, one can prepare field-concentrating features that enhance either electric or magnetic fields. Rather than attempt to gather all of the super-resolution information simultaneously (as one would do in a traditional imaging system), near-field microscopes employ pixel-by-pixel scanning. In this way the signal is acquired from only a small part $\sim D$ of the sample at one time. This scanning method is tedious and slow, but effective. Here we discuss some general principles of microwave microscope design illustrated through an historical review of the field.


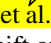
2.1 Early Microwave Microscopes

The original idea of near-field microscopy is often attributed to Synge [21], who proposed using an opaque screen with a small sub-wavelength diameter hole (10 nm in diameter), held about 10 nm above the surface of a smooth flat sample. An optically transparent sample was passed just beneath this aperture, and the transmitted light is collected in a point-by-point scan and raster fashion. This theoretical paper was decades ahead of its time in terms of the technology required to carry out the experiment. Detailed calculations of the field distribution near the aperture were later done by Bethe [24] and Bouwkamp [25]. These near fields contain a

large fraction of high-spatial frequency evanescent waves that can lead to deep sub-wavelength spatial resolution [26,27].

Syngé's idea lay dormant in the literature until the late 1950s, when Frait developed the first ferromagnetic resonance (FMR) microwave microscope [3]. Frait recognized that a conventional FMR resonant cavity simply averaged over the properties of a sample placed *inside* the cavity. He inverted the design by placing the sample *outside* the cavity but retaining coupling by means of a small hole (500- μm diameter) in a thin face of a metallic cavity operating at a wavelength of 3 cm (10 GHz). A $\text{Ni}_{78}\text{Fe}_{22}$ ferromagnetic thin-film sample was scanned beneath the hole and showed contrast in the uniaxial anisotropy parameter. Independent and similar results with a 500- μm diameter hole were obtained by Soohoo on a 350-nm-thick Permalloy film at 5.5 GHz [4]. Similar work with manganite ferromagnetic material has been published more recently [28,29].

Ash and Nicholls performed another Syngé-style experiment at microwave frequencies using a quasi-optical hemispherical resonator as the detection system [30]. This experiment utilized the Syngé geometry of a small aperture (1.5 mm diameter) scanned over a sample with a microwave signal at 10 GHz. The sample was harmonically distance modulated at a fixed frequency, and the reflected signal was phase-sensitively detected at this modulation frequency to improve sensitivity to sample contrast. Similar distance modulation techniques are still in use today. This microscope demonstrated contrast sensitivity to metal films on dielectric substrates, as well as bulk dielectrics with dielectric constant differing by only about 10%.

Non-resonant scanned aperture probes were also developed in the 1960s. In this case a transmission line (coaxial or waveguide) delivers a microwave signal to the probe aperture. The fringe electric and magnetic fields from the aperture interact with the sample. Some part of the signal is stored locally in evanescent and near-zone waves, some is absorbed by the sample, some is reflected back up the transmission line, and some is scattered away as far-field radiation. By monitoring the scattered or reflected signals as a function of probe height and position, an image of the sample response can be made. An early example of this type of scanned probe was developed by Bryant and Gunn [31]. They measured the reflected signal from a tapered open-ended coaxial probe with an inner conductor diameter of 1 mm. The probe was used for quantitative measurements of semiconductor resistivities between  and 100 $\Omega\text{-cm}$. A similar, but resonant, method was developed by Bosisio  et al. to measure the moisture content of paper using measurements of the phase shift of a scanned resonant coaxial probe [32].

The development of near-field optical microscopes using optical waveguides beyond cutoff [33,34] spurred the development of new microwave microscopes. The first of these microwave systems was developed by Fee, Chu and Hänsch by measuring the reflected signal from a non-resonant open-ended coaxial probe [35]. Although similar in design to the probe of Bryant and Gunn, this paper was the first to present the results in the language of near-field microscopy. They employed a 500- μm -diameter center conductor coaxial probe which was extended and sharpened to a tip with 30 μm radius. Operating at 2.5 GHz, they measured the

phase of the reflected signal as a function of position over the sample. An image of copper grid lines showed a spatial resolution of about $30 \mu\text{m}$ (or $\lambda/4,000$). Other microscopes based on a scanned aperture waveguide structure were developed by Golosovsky *et al.* [36,37] and Bae *et al.* [38,39].

2.2 Aperture-Based Probes and Apertureless Probes

The design of near-field probes can basically be divided into two main categories. The first are aperture-based probes, essentially described by Syngde in his seminal paper [21]. The idea is to create a very small interaction volume between the probe and sample by simply constraining the lateral extent of the probing field by means of a sub-wavelength aperture (see Figure 1(a,e)). An alternative approach is to allow a propagating wave to irradiate some large portion of the sample, but to employ a field-concentrating feature, e.g., tip, to enhance the probe-sample interaction locally (Figure 1(b) and Figure 2, inset). The latter apertureless probe design usually results in much stronger signals, albeit with a large background signal.

The designs of Syngde, Frait, Soohoo, and Ash and Nicholls are classic aperture-based approaches to microwave microscopy. The designs of Bryant and Gunn, and Fee, Chu, and Hänsch are prototypical apertureless or field-concentrating

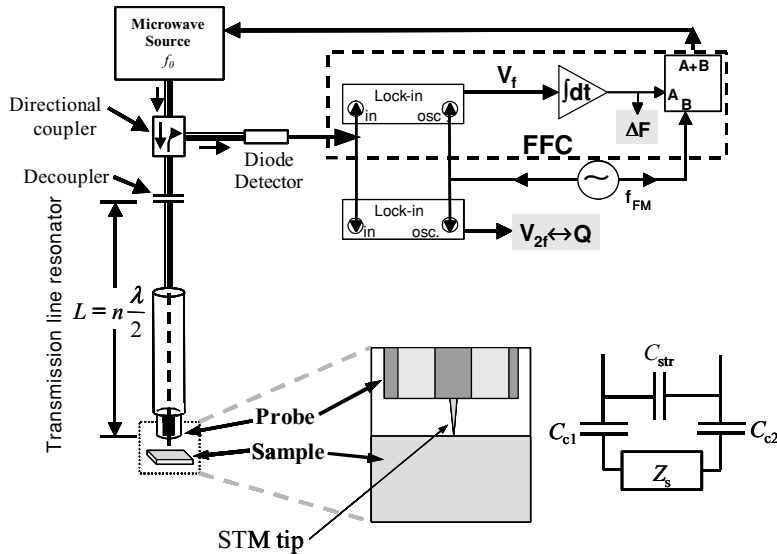


FIGURE 2. The key components of a typical near-field microwave microscope are shown schematically in this figure. The FFC feedback circuit consists of an integrator, and adder circuit. Two output signals are generated: the frequency shift ΔF and the $2f_{\text{FM}}$ voltage, $V_{2f} \propto Q$. The insets show a close view of the coaxial probe, STM tip and sample, as well as a lumped element circuit model for the tip-sample interaction.

designs. In general, the field-concentrating objects are sharp tips, such as those used for STM or AFM. The electric fields between a sharp tip and a flat sample with high permittivity can be greatly enhanced due to the induced image of the probe, thus leading to strongly localized measurement of sample properties. STM-tip field-concentrating features have been employed by many authors [12,40–59] at microwave frequencies, and [60] at far-infrared frequencies. Although the field strengths can be large, the effects of local sample heating are a concern. In at least one case local heating has been shown to be negligible [61]. AFM tip field concentration has been accomplished by a number of groups [62–66]. There have also been efforts to combine an aperture probe with a field-concentrating feature through a tip on an aperture [67], and a waveguide aperture with a tip projection [68]. There is also interest in creating concentrated microwave magnetic fields in a small area of the sample. Seminal work on superconducting quantum interference device (SQUID) microscopy at RF, microwave, and millimeter-wave frequencies showed that this was possible [69,70]. Work with enhanced magnetic field probes was also used to study the local magnetic permeability of materials [16], and localized superconducting nonlinearities [71–75].

2.3 Operating Modes

Microwave microscopes can be operated in one of several detection modes. Non-resonant microscopes typically involve measurements of reflection and/or transmission at a fixed frequency chosen to maximize the signal level at the sample [36,52,53]. Resonant microscopes can be operated in either a fixed-frequency mode [76], with probe/sample distance modulation [77], or with a feedback system to stabilize the source frequency to the variable resonant frequency of the probe/detector system [12,14].

The fixed-frequency resonant mode involves monitoring the reflection or transmission properties of the resonator at a point of maximum slope of the response curve. As the sample properties change, the stored energy and dissipated power in the resonant detection system change. This in turn changes the resonant frequency and quality factor of the detection system. By simply monitoring the off-resonant response (through the reflection coefficient S_{11} , or the transmission coefficient S_{21}), these systems are sensitive to small changes in sample properties.

Because a resonant microwave microscope produces two independent streams of data (e.g., frequency shift and quality factor change, or magnitude and phase, or resistance and reactance), it is advantageous to develop a method to measure both quantities simultaneously. The most common method to do this uses a feedback circuit (such as a phase-locked loop) to force the microwave source to “follow” the time-dependent resonant frequency of the detection system [14], as discussed in section 3. A related technique continuously modifies the distance between the probe and sample to keep the microscope resonant frequency locked to that of a synthesized microwave source [78].

2.4 *Tip-Sample Distance Control in Microwave Microscopy*

One of the strengths of near-field microscopy of any kind is that measurements can be made without any physical contact between the near-field tip and the sample or device under test. However, this requires that the separation between the tip and the surface of the sample be small compared to the characteristic tip size, and that it be kept constant. The precision of any near-field measurement is directly related to the precision with which the tip-sample distance can be maintained, and a good rule of thumb is that the tip should be held reliably at a distance above the sample that is less than one-tenth of the tip size D . Although the absolute value of the mean height is not critical (provided that it meets the criteria above), the variance must be less than 1% of the tip size in order to obtain high precision measurements. For example, for a tip with a characteristic size of $0.1\ \mu\text{m}$, the tip-sample separation will have to be maintained at approximately 10 nm, with a precision of $\pm 1\ \text{nm}$. There are a limited number of techniques that can achieve this precision. Possible solutions that have been employed on various microwave microscopes include shear force, as used in near-field scanning optical microscopy (NSOM), atomic force microscopy (AFM), scanning tunneling microscopy (STM), and height modulation. The challenge is integration of each technique with a suitable near-field microwave microscopy probe. Each of these distance control mechanisms is discussed briefly below, with reference to microscopes on which they have been employed.

2.4.1 Shear Force Based Distance Control

Shear force is a distance control mechanism that was developed for use in near-field scanning optical microscopy (NSOM) [79,80]. The basic idea is that an optical fiber is flexible and can therefore be mounted onto and dithered by a piezoelectric element or a quartz tuning-fork oscillator (TFO) [81] with amplitude from a few nanometers down to a few angstroms. As the tip of such a fiber is brought into close proximity to the sample surface, the amplitude and frequency of the tip oscillations are changed by interactions between the tip and the sample surface. The motion of the tip is detected optically or electrically and a feedback loop allows for precise distance control down to 1 nm. In addition, the height at which this control can be performed is a function of the amplitude of the oscillation—the smaller the amplitude, the smaller the control distance. It has been demonstrated that this type of force feedback can be effectively applied to probe structures other than optical fibers, making it applicable for use in near-field microwave microscopy [15,82,83].

2.4.2 Atomic Force Based Distance Control

Atomic force microscopy (AFM) is an established technique for measuring surface profiles with atomic resolution. In the simplest embodiment, a cantilever is fabricated with a small cone-like tip at one end. This tip is brought into close proximity to the sample surface, and the displacement of the cantilever caused by the repulsion force between the tip and the sample is measured using an optical beam deflection technique as the tip is scanned over the surface. In order to enhance

AFM sensitivity and decrease the tip pressure on the sample, a so-called tapping mode is usually employed. The AFM approach allows for atomic-scale lateral resolution and sub-nanometer precision in height control. AFM distance control has been used to image ferroelectric domains at 1.3 GHz [84]. Microwave transmission lines have been successfully integrated onto traditional AFM cantilevers [66,85].

2.4.3 Scanning Tunneling Based Distance Control

Scanning tunneling microscopy (STM) is a well-established technique for surface studies of conducting, semiconducting and superconducting samples with atomic or near atomic resolution [86]. The conducting probe is brought near the sample (with dc bias applied to either the tip or the sample) at a nominal distance of one nanometer, so that a quantum mechanical vacuum tunnel junction can be established between the tip and the sample. With a fixed voltage applied between the tip and the sample, the quantum mechanical tunnel current decays exponentially as the tip-to-sample distance is increased. It is this exponential decay of current with distance that makes STM sensitive enough for atomic scale imaging [87]. Integrating a near-field microwave microscope with constant tunnel current mode STM allows for distance control. During surface scanning the STM tip remains close to the surface (maintaining the nominal height of 1 nm) and the same tip can be used to perform near-field microwave microscopy. As previously mentioned in section 2.2, a number of researchers have employed STM-based microwave microscopes.

2.4.4 Height Modulation Distance Control

A number of microwave microscopes have employed some form of the height-modulated distance control [88–92]. The general principal is that the tip-sample separation is modulated with fixed amplitude (greater than the separation for tapping mode) and frequency, and the modulated signal is used to control the separation. In one embodiment [78] the tapping mode has been combined with frequency modulation to dramatically improve sensitivity and signal-to-noise ratio of images, resulting in enhanced spatial resolution.

3 Detailed Description of One Microscope

We discuss one class of microwave microscope in some detail to illustrate the basic operation. The essential elements of this microscope (shown in Figure 2) are a microwave source, a coaxial resonator coupled to the microwave generator (either via a decoupling capacitor or inductor), a detector to measure the reflected signal from the resonator, and a frequency-following circuit (FFC).

Figure 2 shows the circuit diagram of the microscope. The generator creates a time harmonic signal that is sent to the microscope resonator. The resonator used is a coaxial transmission line, which is capacitively coupled (via a decoupling capacitor) to the feedline on one side and couples to a sample on the other side.

One particular transmission line used is 2.16 mm in outer diameter with a 500- μm diameter inner conductor (standard 0.085-in. coaxial cable). The inner and outer conductors are copper and the dielectric material used is Teflon. A field-concentrating feature, such as an STM tip (Figure 1(b)), can be added to the center conductor.

The transmission line resonator response is measured in reflection using a directional coupler that allows the signal from the source to reach the resonator and the reflected signal from the resonator to be directed to the diode detector. The diode detector converts the measured power at microwave frequency into a voltage signal (this output, V_{diode} , is proportional to the input microwave power in the range of power of interest). The microwave generator is frequency modulated at a rate f_{FM} to run the FFC. The diode voltage signal is sent to two lock-in amplifiers that phase-sensitively detect the microscope resonator response at the modulation frequency f_{FM} and twice the modulation frequency $2f_{\text{FM}}$. The primary function of the FFC is to keep the generator locked onto the resonant frequency of the resonator. The $2f_{\text{FM}}$ lock-in measures the curvature of the $V_{\text{diode}}(f)$ curve, and gives an output that can be related to the quality factor of the resonator, Q [14,93,94].

The inset of Figure 2 presents a simple model of tip-to-sample interaction (in terms of a lumped-element model), and is discussed further in the next section. This resonator has been integrated onto the probe arm of an Oxford Instruments STM probe. An STM feedback loop was also incorporated into the microscope so that the probe-sample distance control could be maintained through a constant tunnel current while scanning [57,59].

4 Theory of Near-Field Microwave Microscopy

The electrodynamic properties of the sample under study, such as complex permittivity and permeability, affect the detection system parameters such as reflection/transmission coefficient, quality factor, and/or resonant frequency. The ultimate goal for theoretical analysis of a near-field microwave probe is to find a relationship between these detectable quantities and the sample properties. The theoretical study can often be broken in two parts: the sample-to-tip interaction and the tip-to-circuit interaction. The former can be treated within either a lumped element or full-wave/evanescent approach, while a theoretical model for the detection circuit depends on its geometry and can be a lumped element, transmission line, cavity perturbation, or other approach. Below we review some of these approaches, present a novel lumped element model for the sample-to-tip interaction, and obtain general analytical expressions relating the detectable probe parameters to the sample properties in the common case of a detection circuit formed by a transmission line resonator.

4.1 Lumped Element Model for Sample-to-Tip Interaction

Consider the near-field tip as a two-terminal, linear, passive system (e.g., antenna) connected to the detection apparatus such as a transmission line, LC-oscillator,

etc. If the sample is lossless and only the near-zone and/or evanescent field exists beyond the plane of the terminals, then no real power is transmitted into the sample. Such fields store reactive energy, however, and therefore the tip is seen as a reactance by the probe detection circuit. If the sample and/or tip are lossy, then some of this energy dissipates and the impedance gains a resistive part. Thus the interaction between the sample and the probe can be described in terms of the lumped element impedance $Z_t = R_t + iX_t$. Generally, Z_t depends on the tip geometry, the sample electrodynamic properties, and the tip-sample distance. The complex Poynting theorem yields the following expression for the reactance of the near-field tip (e.g., electrically small antenna) [17]:

$$X_t = \frac{4\omega}{|I_i|^2} \int_V (w_m - w_e) d^3x \quad (1)$$

where I_i is the harmonic input current at the tip terminals (such that input voltage $V_i = Z_t I_i$), $w_m = \mathbf{B} \cdot \mathbf{H}^*/4$ and $w_e = \mathbf{E} \cdot \mathbf{D}^*/4$ are the magnetic and electric energy densities, respectively, and the integral is taken over the entire volume beyond the plane defined by the terminals (e.g., the probe sampling volume). Depending on the dominant type of reactive energy stored in this field, the tip is considered either *electric* or *magnetic*. The real part of the tip impedance, R_t , can be due to conduction losses (Joule heat) and electric and magnetic absorptive dissipation in the sample and/or the tip [17,20]:

$$R_t = \frac{\omega}{|I_i|^2} \int_V \left(\frac{\sigma}{\omega} |\mathbf{E}|^2 + \varepsilon_0 \varepsilon'' |\mathbf{E}|^2 + \mu_0 \mu'' |\mathbf{H}|^2 \right) d^3x \quad (2)$$

as well as conventional far-field radiation generated by the tip (i.e., radiation resistance) that can often be neglected for most near-field tips. Note that expressions similar to Eqs. (1) and (2) can be derived for the tip complex admittance as well [17].

4.1.1 Impedance of an Electric Tip

Generically, the impedance Z_{tE} of an electric tip formed by the open end of a two-conductor transmission line (e.g., flush open, terminated with STM tip, etc.), can be represented as a network of the tip-to-sample coupling capacitance $1/C_c = 1/C_{c1} + 1/C_{c2}$, the sample “near-field” impedance Z_s , and the tip stray capacitance C_{str} , (Figure 2, inset):

$$(Z_{tE})^{-1} = \left(\frac{1}{i\omega C_c} + Z_s \right)^{-1} + i\omega C_{str} \quad (3)$$

Z_s is due to the energy stored and/or dissipated in the sample under test, and can be found by integrating Eqs. (1) and (2) over the entire *sample* volume (see, for example, [95]). Both C_c and C_{str} depend on the tip-sample distance h . To obtain high enough sensitivity to the sample properties (i.e., to make $Z_{tE} \sim Z_s$), it is imperative to have both $1/\omega C_c Z_s$ and $\omega C_{str} Z_s$ much smaller than or at least on the

order of unity, which can typically be achieved by making $h \ll D$, where D is the characteristic tip size (see section 1.1).

Under the above conditions let us estimate the near-field impedance due to a homogeneous bulk sample, Z_{sb} , while assuming the true near-field situation $|k_s|D \ll 1$, $k_s = \omega(\epsilon_0\epsilon_s\mu_0)^{1/2}$. Due to its static nature, the sampling near-field occupies a volume governed by D , and the integral in Eq. (1) is on the order of $-\epsilon_0\epsilon'|E_0|^2D^3$, where $|E_0| \sim V_i/D$ is an estimate for the average electric field in the sample. Then Eqs.(1) and (2) yield for $Z_{sb} = R_{sb} + iX_{sb}$,

$$Z_{sb} \approx \frac{1}{i\omega\epsilon_0\epsilon_s D} \quad (4)$$

which is basically the impedance of a capacitor with a geometrical capacitance $\epsilon_0 D$ filled up with material of complex relative permittivity $\epsilon_s = \epsilon' - i\epsilon''$. Let us illustrate this concept for variety of materials.

Dielectric. If the sample is a low-loss dielectric with $\epsilon_s = \epsilon'(1 - i \tan \delta)$, $\tan \delta \ll 1$, then the near-field impedance is

$$Z_{sb} = \frac{\tan \delta}{\omega\epsilon_0\epsilon' D} - i \frac{1}{\omega\epsilon_0\epsilon' D} \quad (5)$$

Its reactive part is capacitive and the probe is sensitive to the sample dielectric constant as well as the loss tangent ($\tan\delta$).

Semiconductor. At microwave frequencies semiconductors can exhibit $\epsilon' \sim \epsilon'' = 1/\epsilon_0\omega\rho$, i.e. contributions from the two conduction mechanisms, displacement and physical, are comparable. Then

$$Z_{sb} = \frac{1}{D/\rho + i\omega\epsilon_0\epsilon' D} \quad (6)$$

so the sample resistance and reactance are of the same order. The sample reactance is again capacitive in this case.

Normal metal. A conductive metal can be characterized by the relative permittivity $\epsilon_s = \epsilon_{nm} \approx -i/\epsilon_0\omega\rho$. Thus Z_{sb} represents the dc resistance of the tip sampling volume:

$$Z_{sb} = \rho/D \quad (7)$$

Unlike the conventional surface impedance of a bulk metal (see [96]), Z_{sb} has *no* reactive part because the geometrical inductance is negligible in the case of an electric probe. Eq. (7) ~~is an implication of the fact~~ that when D is much smaller than the metal skin-depth the probe spatial resolution is governed by the tip size rather than the sample skin-depth. This creates a unique opportunity for near-field microwave microscopy to study just the subsurface portion of the material, unlike conventional far-field techniques that are sensitive to the entire skin-depth layer.

220 Steven M. Anlage, Vladimir V. Talanov, and Andrew R. Schwartz

Plasma. In alternating electromagnetic fields some materials can be conveniently characterized by a plasma-like permittivity [96]:

$$\epsilon_p = 1 - \frac{\omega_p^2}{\omega(\omega - i\nu)} \quad (8)$$

where ω_p is the plasma (or Langmuir) frequency, and ν is the collision frequency. One example is a *superconductor* with a permittivity at frequencies up to ~ 100 GHz and temperatures below $\sim 0.95T_c$ given by [97]

$$\epsilon^{sc} = -\frac{1}{\epsilon_0\mu_0\omega^2\lambda_{sc}^2} - i\frac{\sigma_1}{\epsilon_0\omega} \quad (9)$$

Here λ_{sc} is the magnetic penetration depth, σ_1 is the normal conductivity, and $1/\epsilon_0\mu_0\omega^2\lambda_{sc}^2 \gg \sigma_1/\omega\epsilon_0$ (i.e. the response is dominated by the superconducting carriers). Then the near-field sample impedance of a superconductor is

$$Z_{sb} \approx i\omega\mu_0\frac{\lambda_{sc}^2}{D} \quad (10)$$

Unlike the cases of a dielectric and semiconductor, the near-field reactance of a superconductive sample is *inductive* because the probe is sensitive to the *kinetic* inductance of the superconducting carriers, while again there is no geometrical inductance in Eq. (10).

Another situation when the tip-sample interaction can be described in terms of the lumped element impedance arises if the tip size is such that $|k_s|D \gg 1$ but $|k_0|D \ll 1$. Then $Z_s = G \cdot Z_{sur}$ in Eq. (3), where $G \sim 1$ is the tip-dependent geometrical factor, and Z_{sur} is the sample complex *surface* impedance. The typical example is a flush open coaxial tip (see Figure 1(d)) above a bulk metal or thin non-transparent metallic film. In this case the tip impedance is

$$\begin{aligned} Z_t &= \frac{1}{i\omega C_c} + Z_{sur} \frac{1}{2\pi} \ln \frac{r_{diel}}{r_{in}} \\ &= \frac{d}{i\omega\epsilon_0\pi r_{in}^2} + \frac{d}{i\omega\epsilon_0\pi(r_{out}^2 - r_{diel}^2)} + Z_{sur} \frac{1}{2\pi} \ln \frac{r_{diel}}{r_{in}} \end{aligned} \quad (11)$$

where Z_{sur} is the surface impedance in the case of a bulk sample and the effective surface impedance [98,99] in the case of a thin-film sample, and r_{in} , r_{diel} , and r_{out} are the outer radii of the inner conductor, dielectric, and outer conductor, respectively. The above equation holds for small tip-sample distances $h \ll r_{in}$, $r_{out} - r_{diel}$ which is typically the case for $h \ll D$.

4.1.2 Impedance of a Magnetic Tip

In the case of $|k_s|D \gg 1$ the lumped element impedance of the magnetic tip can be obtained by the method of images [16,100]:

$$Z_{tM} = i\omega L_0 + \frac{\omega^2 M^2}{Z_s + i\omega L_1} \quad (12)$$

where L_0 is the loop self-inductance, L_1 is the sample effective inductance, M is the tip-sample mutual inductance (e.g., tip-to-sample coupling), and Z_s is the sample surface impedance. Away from the sample the tip impedance approaches $i\omega L_0$.

4.2 Transmission Line Model of the Probe

When a transmission line terminated with either an electric or magnetic tip forms a near-field microwave probe, the tip-sample system can be treated as a discontinuity in this line. Consider a near-field tip with impedance Z_t terminating the probe transmission line of characteristic impedance Z_0 . The impedance of a substantially electric tip should satisfy the condition $|Z_{tE}| \gg Z_0$, while for a substantially magnetic tip $|Z_{tM}| \ll Z_0$. Then the complex reflection coefficient from the electric tip can be found as follows:

$$\Gamma_E = |\Gamma_E| \exp(i\theta_E) = \frac{Z_{tE} - Z_0}{Z_{tE} + Z_0} \cong \exp\left(-\frac{2Z_0 R_{tE}}{R_{tE}^2 + X_{tE}^2}\right) \exp\left(i\frac{2Z_0 X_{tE}}{R_{tE}^2 + X_{tE}^2}\right) \quad (13)$$

and the reflection coefficient from the magnetic tip is

$$\Gamma_M = |\Gamma_M| \exp(i\theta_M) = \frac{Z_{tM} - Z_0}{Z_{tM} + Z_0} \cong -\exp\left(-\frac{2R_{tM}}{Z_0}\right) \exp\left(-i\frac{2X_{tM}}{Z_0}\right) \quad (14)$$

To obtain the exponential forms in the right hand side above we used the approximation $(1-x)/(1+x) \approx \exp(-2x)$, which is better than 1% accurate for $x < 0.25$. Note, that an equation similar to Eq. (13) can be written more conveniently in terms of the tip admittance, in which the phase and magnitude dependences on the conductance and susceptance separate like those in Eq. (14) for a magnetic tip.

In order to validate our lumped element model, we compare it to results of numerical modeling for the near-field tip geometry shown in Figure 3(a) and for two types of samples: Si wafers with and without implants. As will be discussed below, both the bulk Si resistivity and the implant sheet resistance were varied. The tip was formed by the open end of a parallel strip transmission line (see Figure 1(e)) that consists of two metallic electrodes supported by a rectangular quartz bar (see [15]). For the purposes of modeling the tip size was on the order of 100 μm , and the tip-sample separation was 250 nm. The modeling was performed using Ansoft's High Frequency Structure Simulator (HFSSTM), a full-wave high-frequency 3D finite element modeler (FEM).

To find the reflection coefficient for the case of bulk Si we substitute Eq. (6) into (3) and the result into (13), which yields the real and imaginary parts of the complex reflection coefficient as a function of the Si bulk resistivity. We are also able to extract these two quantities from the FEM. This modeling was performed for a variety of probe sizes, and representative results are shown in Figure 3(b), where the Si resistivity ranges from 0.01 to 1000 $\Omega\cdot\text{cm}$. It is clear that over a wide range of Si resistivities, the lumped element model agrees exceptionally well with

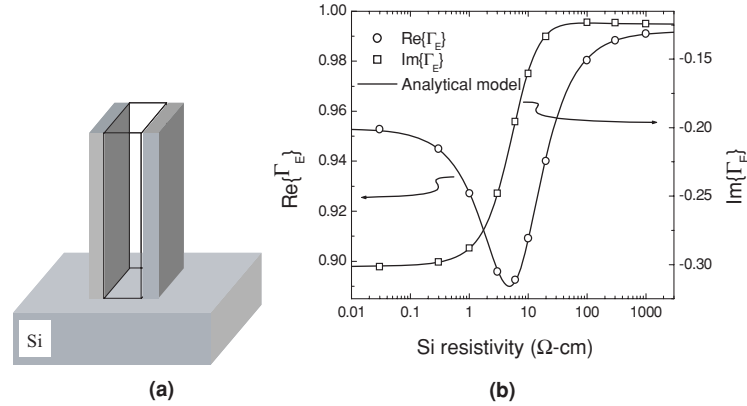


FIGURE 3. (a) Parallel strip transmission line probe. (b) Comparison of analytical lumped element model and finite element numerical data at 4 GHz for the real and imaginary parts of the reflection coefficient as a function of silicon resistivity for bulk Si wafers. The open symbols are the results of the FEM and the lines are fits to the FEM data using the lumped element analytical model, as described in the text.

the FEM. The two free parameters used to fit the lumped element model to the FEM data are D and C_c , while the characteristic line impedance Z_0 was obtained from 2D modeling of the strip-line cross-section. By fitting data for various tip sizes we find that the characteristic tip size D is governed by the entire cross section of the tip. In addition, C_c was found to be in good agreement with the parallel plate capacitor estimate.

Next we included a 0.5- μm -thick implanted layer on top of the Si wafer to study the response of the probe as a function of the implant sheet resistance R_{sh} . The wafer resistivity ρ_{sub} was fixed at 20 $\Omega\text{-cm}$ in this case and Z_{sub} is given by Eq. (6). The lumped element model shown in Figure 4(a) now includes the implant impedance $Z_{\text{imp}} = G \cdot R_{\text{sh}}$, where $G \sim 1$ is the geometrical coefficient dependent on the probe geometry (e.g., see Eq. (11) for the coaxial probe). The results for both lumped element and FEM are shown in Figure 4(b). Again, the agreement between them is excellent over the range of implant sheet resistances from 100 to 800 Ω/sq . In this case the values of D and C_c were fixed as determined from the fitting of FEM data for bulk Si, and the geometrical coefficient G was the only fitting parameter. The fact that the FEM data can be fit so well with only a single fitting parameter is indicative of the robustness of the model and also of the fact that both D (\sim tip cross section) and C_c depend only on the tip geometry and tip-sample separation.

4.3 Resonant Transmission Line

To increase the measurement sensitivity many microwave microscopes employ a distributed circuit resonator which reduces the impedance mismatch, $|Z_{\text{IE}}| \gg Z_0$ or $|Z_{\text{IM}}| \ll Z_0$, between the tip and the probe feed line. Using standard transmission

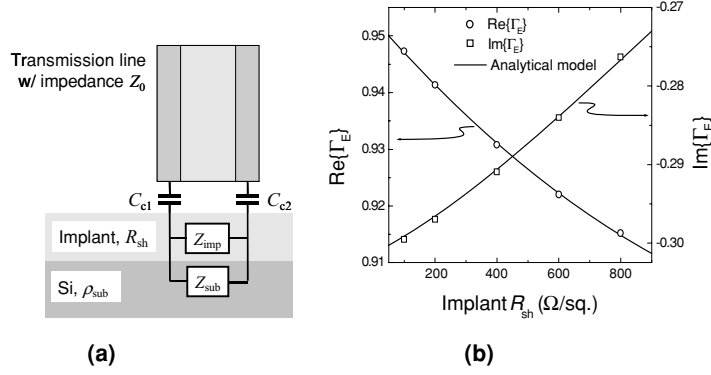


FIGURE 4. **(a)** Lumped element model for implanted Si in the case of implant thickness $t_{\text{imp}} \ll D$, $|k_{\text{imp}}|D \ll 1$ and $|k_{\text{sub}}|D \ll 1$. **(b)** Comparison of the lumped element model and high frequency finite element numerical data for the real and imaginary parts of the reflection coefficient as a function of the implant sheet resistance for implanted Si wafers with bulk resistivity of $20 \Omega\text{-cm}$. The open symbols are the FEM data and the lines are fits to the FEM data using the analytical model.

line theory, one can solve for the voltage at any point in the microscope, including an external detector [76,101,102]. Such models can include many details of the microscope design and are very successful at reproducing its gross and fine properties. The disadvantage of such models is the lack of clear intuitive analytical expressions for the measured quantities. Here we suggest an approach that provides general analytical expressions relating the sample electrodynamic properties to the probe resonant frequency and Q -factor.

The resonant condition of a transmission line resonator can be written as follows [103]:

$$\exp(-i2hL) \Gamma \Gamma_0 = \exp(-i2\pi n) \quad (15)$$

where L is the resonator length, $h = h' - ih'' = \omega(\epsilon_0 \epsilon_{\text{eff}} \mu_0)^{1/2} - ih''$ ($h' \gg h''$) is the transmission line complex propagation constant, ϵ_0 is vacuum permittivity, μ_0 is vacuum permeability, ϵ_{eff} is the effective dielectric constant of the transmission line, Γ is given by Eq. (13) or (14), Γ_0 is the complex reflection coefficient from the resonator opposite end (i.e., short, open, or coupling impedance), and $n = 1, 2, \dots$ is the mode number. As an example consider an electric tip terminating a half-wavelength resonator. Substitution of $\Gamma_0 = 1$ and (13) into (15), using the complex angular frequency $\omega = \omega' + i\omega''$, and separating the real and imaginary parts yields the following expressions for the probe resonant frequency $F = \omega'/2\pi$ and the unloaded Q -factor:

$$F = \frac{\pi n}{2\pi L \sqrt{\epsilon_0 \mu_0 \epsilon_{\text{eff}}}} \left[1 + \frac{Z_0 X_{\text{tE}}}{\pi n (R_{\text{tE}}^2 + X_{\text{tE}}^2)} \right] \quad (16)$$

$$Q = \frac{\omega'}{2\omega''} = \left(\pi n + \frac{Z_0 X_{\text{tE}}}{R_{\text{tE}}^2 + X_{\text{tE}}^2} \right) / \left(2h'' L + \frac{2Z_0 R_{\text{tE}}}{R_{\text{tE}}^2 + X_{\text{tE}}^2} \right) \quad (17)$$

224 Steven M. Anlage, Vladimir V. Talanov, and Andrew R. Schwartz

From Eq. (16) one can find the relative shift in the probe resonant frequency versus change in the tip capacitance C_t for a low-loss sample as follows:

$$\frac{\Delta F}{F} = -\frac{Z_0}{L\sqrt{\epsilon_0\mu_0\epsilon_{\text{eff}}}}\Delta C_t \quad (18)$$

Equation (18) provides an estimate for the microscope's sensitivity to changes in the tip capacitance. For typical probe parameters $L \sim 1$ cm, $Z_0 \sim 50 \Omega$, $\epsilon_{\text{eff}} \sim 2$ and typical precision in $\Delta F/F$ measurement ~ 0.1 ppm, ΔC_t is on the order of 10^{-19} F = 100 zF. Capacitance resolution down to a few zepto-Farads has been demonstrated in state-of-the-art experiments [104].

According to Eq. (17) there is a small change in the Q -factor due to change in the probe resonant frequency ω' . In practice however, the losses are not uniform in the transmission line, i.e., h'' depends on z . In this case there will be an extra change in Q due to redistribution of the resonator currents near the tip (see also [105]), even in the case of a lossless sample.

Using the above approach for the magnetic tip one can obtain expressions similar to Eqs. (16) and (17), which are omitted here due to limited space.

4.4 Lumped Element/Series and Parallel Models

Lumped element models are useful for understanding the properties of a single resonance of the microscope. The simple inductor-resistor-capacitor (LRC) series or parallel models have proven successful for generating simple intuitive formulas for microscope behavior [89,106–108]. The tip impedance Z_t should be added in parallel with the capacitor for electric probes [77] or in series with the inductor for magnetic probes [16,100].

4.5 Full-Wave Analysis

If the near-field tip forms a discontinuity in the probe transmission line or waveguide it can be analyzed by the modal analysis technique [20] from which the equivalent lumped element circuit for the discontinuity can be derived using one of the standard discontinuity representations [109]. Then one can proceed to Eqs. (13) and (15) to relate the sample electrodynamic properties to the probe detectable quantities.

Another way to carry out a full-wave analysis is to use numerical simulations of the problem [59,100]. One example is shown in Figure 5 where the fringe electric field near the open end of a parallel strip transmission line (see Figure 1(e)) was simulated using Ansoft's HFSSTM, a full-wave 3D finite element modeler of Maxwell's equations. The parallel strip transmission line is formed by 1- μm -thick and 4- μm -wide metallic strips separated by a 4- μm -thick quartz dielectric. Figure 5(a) shows the E -field in the case when no sample is present, i.e., the sample being vacuum. In Figure 5(b) the tip is placed 100 nm above a bulk Si sample with

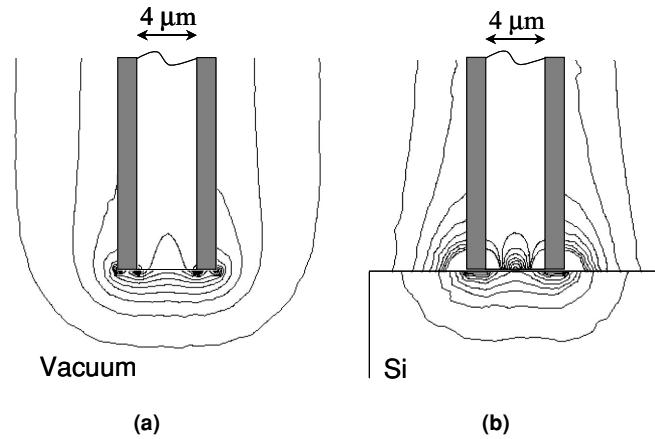


FIGURE 5. Numerical simulation of the fringe electric field at 5 GHz near the open end of the parallel-plate strip-line probe for (a) vacuum and (b) 0.01 Ω -cm resistivity Si samples. The solid lines are intensity contour plots of the E -field magnitude.

resistivity 0.01 Ω -cm. Such a resistivity at 5 GHz provides $\epsilon' \ll \epsilon'' = 1/\epsilon_0\omega\rho$, while the skin-depth is still much greater than the tip size. The solid lines are the intensity contour plots for the E -field. The scale is chosen such that the outermost line indicates where the probing field is reduced by 20 times compared to its maximum value at the sample surface, which differs by almost four orders of magnitude for the two samples. One can see that the field probing depth is basically the same for both samples. It is unaffected by the sample electrodynamic properties and is governed primarily by the tip geometry.

4.6 Cavity Perturbation Approach

Typically, the volume occupied by the probing fields is much less than the overall resonator volume. Thus a cavity perturbation approach [20] can be employed to calculate changes in the resonant frequency and Q -factor of the probe due to its interaction with the sample [105,110]. For example, to calculate changes in the probe resonant frequency F and Q -factor associated with measurement of a low-loss homogeneous electric thin-film of unknown complex permittivity $\epsilon_{\text{film}} = \epsilon'_{\text{film}}(1 - i \tan \delta)$ backed by an arbitrary substrate, one proceeds as follows. Assume that there are two resonant probes that have the same geometry but differ in the sample that is being measured. One sample is the thin-film sample under test, and the other is an air film with relative permittivity $\epsilon_{\text{air}} = 1$ of the same thickness and backed by the same substrate as the film under test. One can then calculate the electric fields in the two cases, assuming that everything else about the measurement is identical. The two field solutions shall be called E_1 and E_2 .

Cavity perturbation theory shows that

$$\frac{\Delta F}{F} \cong -(\epsilon'_{\text{film}} - 1) \frac{\epsilon_0}{4W} \int_{V_s} \mathbf{E}_1 \cdot \mathbf{E}_2 dV \quad (19)$$

$$\Delta \left(\frac{1}{Q} \right) = -\tan \delta \frac{2\epsilon'_{\text{film}}}{\epsilon'_{\text{film}} - 1} \frac{\Delta F}{F} \quad (20)$$

where W is the total energy stored in the resonator, and V_s is the volume of the thin film.

The electric fields \mathbf{E}_1 and \mathbf{E}_2 can be calculated by a number of means. One popular choice is to invoke the electrostatic approximation that holds at distances much less than the wavelength from the source, and use the solutions to Poisson's equation for the electric field. Another choice is to use a Fourier optics decomposition of the fields due to a source (such as a sphere above a plane [111], or an electrically small dipole above an interface [112,113]) and directly calculate $\Delta F/F$ through the integrated Poynting vector. A third approach is to use full-wave numerical solutions to Maxwell's equations (see 4.7) for the perturbation calculation. If only the film loss tangent is to be determined from the experiment then no field solution is required if both $\Delta(1/Q)$ and $\Delta F/F$ are measured simultaneously and ϵ'_{film} is known.

4.7 Spatial Resolution

To discuss the spatial resolution of a near-field probe it is convenient to divide the subject into the *qualitative* (or imaging) and *quantitative* (e.g., metrological) resolutions (see [114]). Empirically, the imaging resolution can be defined as the size of the smallest feature that can be observed on a high contrast sample such as alternating strips of high and low permittivity (e.g., metal/dielectric) or permeability material for electric or magnetic probes, respectively. This concept has been widely employed in practice [57,65] and is somewhat similar to using a Au/C combination to define the ultimate resolution of the scanning electron microscope. The metrological resolution however shall be defined as the size of an area or volume such that the probe response is insensitive to the material properties outside of it. In other words, the volumes that confine, say, 50% and nearly 100% of the energy stored in the probing field determine the microscope's qualitative and quantitative resolutions, respectively. While imaging resolution is generally sample dependent, the metrological one is basically defined by the probe geometry due to the static character of a near-field (see also Figure 5).

The imaging resolution of a near-field microwave probe is typically governed by the probe's smallest feature size such as the curvature of an STM or AFM tip apex. Other authors have discussed features governing microwave microscope spatial resolution as well [59,66,106,115–117]. It has been argued elsewhere [118] that for metallic tips the tip geometry rather than the skin-depth of the tip material is the limiting length scale. Limits in the range of a few nanometers have been discussed by several authors [57,65,88,119]. Such an extreme resolution is generally due to

redistribution of the currents/charges at the tip in the presence of a high permittivity sample where an image of the probe is induced. At the same time, the metrological resolution of apertureless probes could be on the order of a few hundred microns as governed by the length of the entire STM tip wire or AFM cantilever (see Figure 1(b,c)). This is basically due to the energy stored in the probe parasitic stray field or the “non-tip-end field component” [120]. In the STM-tip based resonant probe, for example, this could account for up to 50% [120] of the total frequency shift caused by the sample and therefore, according to the resonant cavity perturbation theory [20], a similar portion of the reactive *probing* energy as well.

To take full advantage of small antenna feature sizes, the tip must be kept as close as possible to the sample surface. Scanning tunneling, atomic force, and shear-force distance control mechanisms or just a mechanical contact can be used to achieve ultra-resolution, as discussed in section 2.4.

4.8 Quantitative Materials Property Imaging

One advantage of near-field microwave microscopy is the ability to image properties of materials in a quantitative manner. This is possible because of the relative simplicity of the physics of electromagnetic interactions with materials at microwave frequencies. There are two approaches to quantitative imaging. The semi-empirical approach employs standard samples of known properties to establish a calibration data set. The properties of unknown samples are then found by converting the measured quantity into the unknown value through some type of interpolation scheme. These methods are best when they are backed up with a model that justifies the calibration and interpolation routine, (see for example [15,93,102,105,121]). The other approach is to rely entirely on calculations of the probe-sample interaction and to work backward from measured results to deduce the unknown sample property (see, for example, [122]). One drawback of such an approach is that it typically requires knowledge of the exact tip geometry and tip-sample separation.

5 Experimental/Empirical Results in Microwave Microscopy

Here we present an overview of experimental results of microwave materials property investigation with scanning near-field microwave microscopes at sub-wavelength resolution between 100 MHz and 100 GHz. The overview is broken down in terms of materials properties, including dielectrics and ferroelectrics, semiconductors, metals, superconductors, and biological specimens.

5.1 Dielectrics and Ferroelectrics

Insulating materials can display interesting and unique polarization dynamics due to their electrically charged internal constituents. They can also be of technological interest for their ability to store information in the form of ferroelectric polarization,

and to serve as either low- or high-dielectric constant materials in wiring networks or capacitors. It is of interest to characterize the dielectric properties of these materials on short length scales because of their use in highly integrated electronics applications. Fundamental materials concerns include the microscopic origins of dielectric response and its sensitivity to defects, the origins of dielectric loss, and the ultimate limit to the size of a stable and switchable ferroelectric domain. Materials issues include the engineering of materials with controlled dielectric response (usually with very high or very low dielectric constant), minimizing dielectric losses, and maximizing ferroelectric polarization, as well as piezoelectric, and magneto-electric effects. Near-field microwave microscopes offer opportunities to investigate all of these properties. We discuss first the localized linear response measurements, followed by the nonlinear response, and finally measurements of dielectric loss.

5.1.1 Linear Dielectric Response

The use of open-ended coaxial transmission lines and resonators to measure linear dielectric response has a very long history [123,124]. The first scanned measurements of dielectric contrast at microwave frequencies used lumped element [64], coaxial [65,125–128], and microstrip resonators [115] but did not extract quantitative measurements of the dielectric constant. Later quantitative modeling of the probe-sample interaction led to the development of quantitative local dielectric constant measurements [12,105,110,120,129–136]. Most of these techniques employ an electric probing tip in contact with the sample. These models relate the sample dielectric constant to the measured frequency shift, and rely on knowledge of the probe and sample geometry, as well as an accurate model of the electric field structure at microwave frequencies. Recently, a novel non-contact technique for dielectric constant metrology of thin films has been developed by Talanov et al. [15]. It requires no knowledge of either the tip geometry or absolute tip-sample distance, while a shear-force distance control mechanism is used to hold the tip in close proximity to the sample.

Most models employed to date assume that the electrostatic field structure is adequate for these calculations, although experimental and numerical work to investigate finite frequency effects is underway [137]. This method of imaging has proven very useful for the evaluation of sample properties in combinatorial dielectric libraries [138–144]. The imaging of combinatorial libraries and phase diagrams has been reviewed in references [145,146].

5.1.2 Nonlinear Dielectric Response

The microscopes developed for linear dielectric response also prove useful for nonlinear dielectric imaging. Because these microscopes use field-concentrating features, such as STM and AFM tips, in contact with the film, a low-frequency electric field can be locally applied to the sample in addition to the microwave electric field. The additional field can influence the dielectric response of the material. This method of imaging was pioneered by Cho, who showed how higher-order

terms in the electric displacement versus electric field $D(E)$ relationship could be measured with a scanning coaxial microscope [64,65]. An important advantage of nonlinear imaging is the fact that the sample response is more and more localized near the tip as higher order nonlinearities are measured [147]. The higher-order dielectric constants are proportional to higher powers of the electric field. Because the near-field decays on a scale on the order of the tip size, these higher powers are more concentrated beneath the tip, both laterally and in terms of depth. However, the higher order nonlinear terms become smaller with increasing order, making the measurements more sensitive to noise. Nonlinear dielectric imaging has also been pursued by other groups [91,110,130,131,148–151], including quantitative results for the higher-order terms in the nonlinear $D(E)$ expansion [110,129,130].

It was also found that the nonlinear dielectric response is sensitive to internal de-polarizing fields in polarized materials. The internal field has the effect of shifting the nonlinear dielectric constant versus applied field curve. The amount of shift is proportional to the local value of polarization, making it possible to image a quantity proportional to polarization. This technique was employed in reference [131] to image ferroelectric domains in periodically poled LiNbO₃, to image locally switched domains of deuterated triglycine sulfate (DTGS), and to image domain formation and coarsening at the paraelectric to ferroelectric phase transition in DTGS at the Curie temperature $T_C \approx 340$ K, as shown in Figure 6 [102,131].

5.1.3 Dielectric Losses

It was shown above that microwave microscopes have the ability to determine losses in a sample through measurement of the quality factor, Q . The minimum value of $\tan\delta$ that can be measured is determined by the ratio of the energies stored in the tip sampling volume and the probe resonator as well as the experimental capability to measure small differences in Q . Eq. (20) shows that for a typical frequency shift $\Delta F/F \sim 10^{-3}$ and state-of-the-art sensitivity in Q -factor measurement $\Delta(1/Q) \sim 10^{-6}$, loss tangents down to 10^{-3} can be detected.

Many techniques have been developed to measure dielectric loss in stationary conditions on bulk samples [123]. A scanned probe measurement of dielectric loss was first presented by reference [105], where they measured dielectric loss values between 1.5×10^{-3} and 5×10^{-1} in oxide single crystals, and between 0.01 and 0.2 in SrTiO₃ and Ba-Sr-Ti-O thin films. Other researchers have measured loss contrast [128,132,152] and values of $\tan\delta$ as small as 1.4×10^{-3} in yttria-stabilized zirconia [133].

5.2 Semiconductors

Semiconducting materials are intermediate between insulators and metals in that they offer two parallel conduction channels: displacement and physical. As the doping density increases, the two conduction mechanisms can become comparable

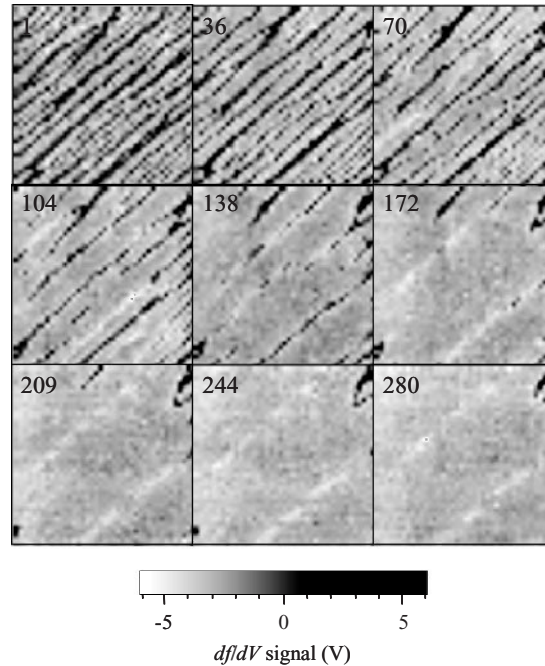


FIGURE 6. Domain formation in a deuterated triglycine sulfate crystal at 320 K. The nonlinear dielectric response images are of the same $100 \times 100\text{-}\mu\text{m}$ region of the sample, at different times following cooling from 380 K (above T_C) to 320 K (below T_C). The signal is proportional to the local vertical component of polarization (down is dark, up is bright). The elapsed time in minutes is shown in the upper left corner of each image. For further details, see references [102,131].

at microwave frequencies (see Eq. (4)). Hence microwave microscopes have been pursued as a sensitive way to measure localized doping profiles in semiconductors.

5.2.1 Linear Response

Some of the earliest work on near-field microwave microscopy was devoted to sheet resistance measurements in semiconductors [31,153] and employed scanned coaxial probes [154,155]. Further work explored high-resolution sheet resistance contrast and imaging [57,77,92,156]. Dopant profiling was done through capacitance imaging [157] and spatially resolved measurements of recombination lifetimes have also been done [107,158,159]. Semiconductor thermography [160] and carrier concentration [107] can be measured through near-field techniques as well.

5.2.2 Nonlinear Response

Semiconductor samples also show a nonlinear response. The applied RF and microwave electric fields can create carrier concentration enhancement or depletion

near surfaces and buried p/n junctions. This has the effect of changing the capacitance between the probe and sample in a way that depends on the instantaneous value and peak amplitude of the applied oscillating electric field. Such variations can give rise to harmonic generation, mixing, or intermodulation of signals in a localized area around the microscope probe. Nonlinear spectroscopy measurements were carried out at high resolution by [46] and [161]. Later [162] demonstrated that the nonlinear response could be used to significantly enhance the spatial resolution of the microwave microscope. Nonlinear semiconductor spectroscopy was also used to image variation of local carrier density in indium tin oxide [117].

5.3 Metals

The imaging of metals by near-field microwave microscopes has been a very fruitful area of investigation. The microscopes are sensitive to probe-sample capacitance and sample topography, sheet resistance of thin films, and spin properties of ferromagnetic metals and impurities.

5.3.1 Capacitance/Topography

Scanning capacitance microscopy (SCM) has benefited greatly from the use of resonant RF and microwave techniques. The earliest use of a “scanning microwave microscope” for topographic and capacitive imaging was the RCA VideoDisk player [163,164]. This instrument used a 1-GHz lumped LC oscillator that employed a metal-coated tip as one part of the capacitor. As the tip moved over the surface of a corrugated disc, the capacitance variations would be detected through variation of the resonant frequency of the circuit, and information could be retrieved from the topography of the disc. The microscope could detect topography on the order of 0.3 nm with a spatial resolution of 100 nm. Other microwave frequency scanning capacitance microscopes have followed from this invention [165–168]. In most cases, the probe-sample capacitance forms part of a capacitor in a resonant lumped LC circuit. One measures the resonant frequency shift as the probe moves over the sample. This can yield sensitivities to changes in capacitance on the order of zepto-Farads, as demonstrated above. Other near-field microwave microscopes have been employed for quantitative topographic imaging [56,57,76,82,101,104,126,169,170]. Generally speaking, scanned microwave dielectric measurements are basically just capacitance measurements combined with detailed knowledge of the probe and sample geometry. The reader can find more on scanning capacitance microscopy in the chapter by J. Kopanski in this book.

5.3.2 Thin Films/Sheet Resistance/Hall Effect

The microwave microscope has found application as a quantitative measurement of metallic thin-film sheet resistance. After early experiments demonstrating contrast from metallic thin films [76,152,153], Steinhauer *et al.* showed that systematic and quantitative results could be obtained for sheet resistance and topography

232 Steven M. Anlage, Vladimir V. Talanov, and Andrew R. Schwartz

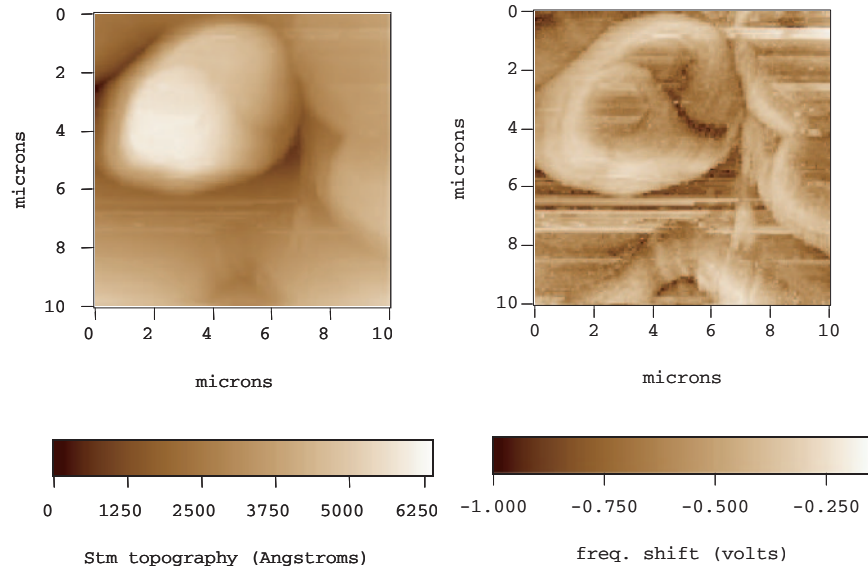


FIGURE 7. STM topography image and frequency shift image of the surface of a $\text{La}_{1.4}\text{Sr}_{1.6}\text{Mn}_2\text{O}_7$ single crystal, taken at 298 K and 7.47 GHz, with a bias of 1 V and tunnel current of 0.5 nA. Sample provided by Y. Mukovskii.

by combining the frequency shift and Q -factor measurements [14,93,121]. Other groups developed microscopes with similar capabilities [68,89,169,171–176], including measurements of thin-film conductivity in ferromagnetic combinatorial libraries [140]. An interesting use of the millimeter-wave waveguide microscope was the measurement of local Hall effect signals [177], and polarization contrast [39,178].


Also of significance is the search for nm-scale inhomogeneity in correlated electron metals such as cuprates and manganites [57,179]. Figure 7 shows an example result from an STM-assisted near-field microwave microscope. The frequency shift image shows distinct contrast from sample property variations that are not present in the STM topography image. These local variations contain information about the local sheet resistance and the microscopic physics of the manganite materials.

5.3.3 Ferromagnets/Permeability

The earliest microwave microscope was used to image ferromagnetic resonance [3,4]. Later generations of microscopes returned to the problem of permeability contrast and magnetic resonance. The scanning SQUID microscope was used to generate microwave and millimeter-wave signals in close proximity to the SQUID. The sample response to the high frequency magnetic fields modified the properties of the SQUID, giving rise to contrast [69,70]. Ferromagnetic resonance probes were employed for eddy current microscopy [180]. Later, reference [16] employed

a scanned loop probe to make quantitative images of magnetic permeability in ferromagnetic and paramagnetic metals. This microscope was also used to perform imaging of ferromagnetic resonance fields in a bulk manganite sample. A resonant slit microscope was also used to measure ferromagnetic resonance in nanoparticles [181]. Ferromagnetic resonance force microscopy was also developed for investigation of very small localized magnetic moments [182,183].

5.3.4 Electron Spin Resonance Microscopy

An exciting use of microwave microscopes is in ron spin resonance (ESR) microscopy [184]. The pioneering work of Ikeya *et al.* on various ESR microscopes covered many applications in biology, medicine, dentistry, and materials [185–190]. An important objective is to detect spin resonance from a single spin in a sample. This ultimate limit has been pursued through an STM tunnel junction [188,189,191,192].

5.4 Superconductors


The interest in high-temperature superconductors since their discovery in 1986 has spawned research on local investigations of their linear and nonlinear response. These microscopes involve the use of a cryogenic environment for the sample, complicating the operation of the instrument. An early microscope could measure variations in the transition temperature of a superconducting film, as well as some temperature dependence of the local microwave losses [193]. Other work was done imaging high- T_c superconductors [73,194–196], including T_c imaging [172], as well as imaging bulk Nb [171,172].

The nonlinear properties of superconductors are important for both fundamental and practical reasons. On the fundamental side, the measurement of an intrinsic nonlinear Meissner response is an important goal. Most measurements of this small nonlinearity are overwhelmed by extrinsic nonlinearities, most of which come from edges and corners of samples where large current densities build up. Early experiments were done to identify the local sources of intermodulation distortion in resonant superconducting devices [197]. Later experiments used a scanned magnetic loop probe to apply a focused local current distribution at points far from edges and defects in the superconducting sample [71–75,198]. These experiments successfully resolved a localized source of nonlinearity (a single grain boundary Josephson tunnel junction) and found results for spatial and power dependence of the nonlinear signals in good agreement with models of the junction.

5.5 Biological Samples

Microwave techniques are attractive for biological applications because of their sensitivity to water and dielectric contrast [95]. Early dielectric measurements on biological samples were carried out by [124,199–201]. Scanned microwave measurements to determine water content and mineral content were carried out by


234 Steven M. Anlage, Vladimir V. Talanov, and Andrew R. Schwartz

Tabib-Azar  *et al.* [66,115,202]. Images were also made of dried DNA [116]. Living biological samples often have to be imaged inside saline solutions. Here, as in semiconductors, there are two parallel conduction channels: displacement currents through the water dielectric (with $\epsilon_r \sim 80$), and conduction current through the salt ions. On a related note, an early use of the STM-assisted microwave microscope was molecular spectroscopy measurements. It was predicted that harmonics due to molecular rotations on a surface would provide unique signatures of molecules [61].

5.6 Parametric Microwave Microscopy

It is of interest to explore the properties of materials at microwave frequencies as a function of other variables or parameters. The dependence of conductivity or dielectric constant on other parameters can give insights into the physical origin of the microwave properties of materials, for example.


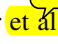
5.6.1 Electric Field

Low-frequency electric fields can be used to modify the structure of polar dielectric materials. These changes will in turn modify the dielectric properties of the material. The measurement of nonlinear dielectric response has been investigated by several groups [64,65,110,117,129,130,147]. The low-frequency electric field is typically applied between a sharp tip in contact with the dielectric and a counter electrode. Field strengths on the order of 10^6 – 10^8 V/cm can be easily applied in thin-film dielectrics. Further, if the material is polarized, it will contain internal depolarization fields. These fields act in a way similar to external bias and shift the nonlinear dielectric versus external bias curves left  or right on the bias voltage axis. Such shifts indirectly measure the local polarization of the material underneath the tip [102,131]. Figure 6 shows an example of local polarization imaging in a ferroelectric crystal.

5.6.2 Magnetic Field

A low-frequency magnetic field can be applied during microwave microscopy to modify the magnetic properties of a sample. For example the magnetic field can be used to induce ferromagnetic resonance (FMR) in the sample at a frequency that matches that of the microwave microscope [3,4,16,28,29]. The work of [16] acquired images of the FMR resonant field as a function of position over a $\text{La}_{0.8}\text{Sr}_{0.2}\text{MnO}_3$ (LSMO) sample in a fixed external magnetic field.

5.6.3 Temperature

The microwave properties of materials can vary dramatically with temperature. For example, phase transitions can occur which cause a change of state and ordering in a material. One example is the ferroelectric  to paraelectric phase transition at the Curie temperature, T_C . Steinhauer  *et al.* have imaged the development of

ferroelectric domains out of a paraelectric background as a deuterated triglycine sulfate sample is cooled through $T_C \approx 340$ K (Figure 6). They observed a peak in the dielectric constant at T_C , and a scaling of the domain sizes (coarsening) using a microscope that can vary the sample temperature from room temperature to 400 K [102,131].

Microwave microscopes have also been developed to study the low temperature microwave properties of materials [57,193,195,196]. Most of this work has investigated superconducting properties, including the transition temperature [193,195], the surface resistance [193], and local nonlinear electrodynamic properties [71–75]. One challenge with these microscopes is motion control at cryogenic temperatures. Solutions include generating the motion at room temperature and transmitting it to the low-temperature environment through mechanical coupling [94,126,171,172,195,197,198,203,204], or to use piezoelectric tubes in the cryogenic environment (see Figure 7) [57].

5.6.4 Frequency

Some physical properties measured at microwave frequencies can be frequency dependent. One example is dispersion of dielectric properties due to the contribution of different polarization mechanisms to the total dielectric response. One approach is to build a tunable resonant detection system [117,175,205] by varying the physical size of the microwave detector resonator. This can also vary the coupling between the microwave source and the microscope. One also has the option with transmission line resonators to excite higher-order resonant modes of the system to perform broadband microwave imaging [76]. This has been employed to perform broadband dielectric imaging of Ba-Sr-Ti-O thin-film samples [137,206].

6 Future Directions

The future of near-field microwave microscopy has many promising directions. We discuss a few of these below.

6.1 Theory

Much remains to be learned about generating near-zone or evanescent fields, how they interact with the sample, and the most efficient ways to control the confining volume and recover the information contained in their high spatial frequency harmonics (see also section 6.7). Another topic of theoretical study is the relationship between the near-zone and evanescent description of the fields generated by the near-field probes. In the area of quantitative measurements the theory of probe-sample interaction for a multilayer, stratified, and/or anisotropic sample is of great importance and such work is already underway [95]. We also believe that approaches developed in conventional antenna theory (see for example [112,207]) as well as the Poynting theorem (see Eqs. (1) and (2)) could be leveraged for this

purpose. For example, they may be employed to determine the conditions when the far-field radiation from the tip can be neglected, which is important for measuring losses in samples.

6.2 Instrumentation

Development of novel probe geometries is necessary to reduce the tip stray capacitance found in many microscopes. This will inevitably improve the sensitivity and spatial resolution of microwave microscopes [208]. Advanced shielding structures for AFM probes are being fabricated [66]. Yet another goal is reduction of the parasitic far-field radiation from the probe, which can be achieved by using balanced quadrupole-like (and higher order) tip geometries [114]. One more open question is the influence of the tip-sample ponderomotive forces on the probe-sample distance control.

6.3 Nano-Imaging

It is clear that microwave microscopes can measure contrast on nanometer length scales, perhaps even quantitatively, and many new scientifically and technologically interesting materials have features on nm scales. For example, magneto-electric nano-composites have very large interface areas between the ferroelectric and ferromagnetic constituents [209]. This can lead to an enhanced magneto-electric effect. Other electrical and mechanical phenomena can be enhanced through nano-engineering of materials, and these would be interesting to investigate locally at microwave frequencies. There is also scientific interest in generating materials contrast on nanometer scales. For example, colossal magneto-resistive materials (see Figure 7) have phase separation into ferromagnetic metallic and charge-ordered insulating regions on nanometer length scales. There are other correlated electron materials that are expected to have similar nano-structure, such as cuprate superconductors. For example, it may also be possible to perform domain wall resonance imaging [210] with microwave microscopes. One concern with nano-imaging is the eventual breakdown of the macroscopic constitutive properties (ϵ and μ) concept [211,212], and the emergence of quantum properties.

6.4 Single-Spin Microwave Microscopy

Further progress on detecting the spin of a single electron through localized electron spin resonance [41,213] will be made. If this capability can be extended to spin-polarized tunneling, then new applications in quantum computing [192,214] and nano-microwave oscillators [215] may be forthcoming.

6.5 Coupling to High-Speed Nanodevices

The microwave microscope offers the opportunity to couple high-speed signals locally to nanodevices such as nano-electromechanical devices (quantum-limited

GHz oscillators) and carbon nanotube transistors. Multi-walled nanotubes are being investigated for use as interconnects in integrated circuits [216]. The microscope is well suited for measurements of the quantum of resistance, inductance, and capacitance in single nanotubes [217]. The microscope can also be used to measure Coulomb blockade tunneling at RF and microwave frequencies in a mesoscopic device [61].

6.6 *Biological Imaging*

Much remains to be learned about the capabilities of near-field microscopes in biological imaging [95,115]. There is a great challenge/opportunity to image living cells in their saline solutions. It is possible to design a microscope that has equal current flow through the dielectric and conduction channels in such solutions. These may be very sensitive to small variations in ion concentration or membrane dielectric properties. There is also interest in applying near-field microwave techniques to localized heating of biological media [218].

6.7 *Metamaterial Near-Field Lenses*

The development of left-handed metamaterials [219] has opened the possibility of new applications in near-field microscopy. One possible new application is that of a near-field flat lens [22,220]. Such lenses take a source in the near-field of a slab of negative index of refraction and convert it into a super-resolution image on the other side, and have been demonstrated at microwave frequencies [221]. In other words, the superlens retains high spatial frequency information in constructing an image. The lens can amplify evanescent waves in a range of wavenumbers, depending on its loss [222]. Integrating such a lens with a near-field microwave microscope may allow further improvements in spatial resolution, or may facilitate new measurements on systems that cannot be studied directly with scanned probes, such as buried features [223]. Another possibility is the manipulation of surface plasmons at microwave and millimeter-wave frequencies [224] to produce enhanced transmission through sub-wavelength apertures [225] for near-field micro- or nano-spectroscopy.

Acknowledgments. We are grateful to R. C. Black, C. Canedy, H. M. Christen, S. Dutta, B. J. Feenstra, T. Hartman, W. Hu, A. Imtiaz, J. Kanner, S.-C. Lee, J. Melngailis, D. Mircea, R. Moreland, Y. Mukovskii, M. Pollak, A. K. Prasad, Y. Qi, R. Ramesh, G. Ruchti, A. Scherz, I. Smolyaninov, D. Steinhauer, A. S. Thanawalla, A. Tselev, C. P. Vlahacos, and F. C. Wellstood for their assistance and fruitful discussions. We also thank M. Golosovsky, A. Reznik, and A. Tselev for critical reading of the manuscript. This work is supported by the National Science Foundation through the UMD MRSEC NSF/DMR-00-80008 and its Microwave Microscope SEF, NSF/GOALI DMR-0201261, and through NIST-ATP No. 70NANB2H3005.

References

1. M. Dressel and G. Grüner, *Electrodynamics of Solids*, Cambridge University Press, Cambridge, 2002.
2. M. Tinkham, *Introduction to Superconductivity*, 2nd Edition, McGraw-Hill, New York, 1996, p. 87.
3. Z. Frait, V. Kambersky, Z. Malek, and M. Ondris, *Czech. J. Phys. B* **10**, 616 (1960).
4. R. F. Soohoo, *J. Appl. Phys.* **33**, 1276 (1962).
5. R. F. Soohoo, *Microwave Magnetics*, Harper & Row Publishers, New York, 1985.
6. E. H. Brandt and G. P. Mikitik, *Phys. Rev. Lett.* **85**, 4164 (2000).
7. S. M. Anlage, D. E. Steinhauer, B. J. Feenstra, C. P. Vlahacos, and F. C. Wellstood, "Near-Field Microwave Microscopy of Materials Properties," in *Microwave Superconductivity*, ed. by H. Weinstock and M. Nisenoff, (Kluwer, Amsterdam, 2001), p. 239. Also available at <http://arXiv.org/abs/cond-mat/0001075>.
8. X.-D. Xiang, C. Gao, *Mat. Character.* **48**, 117 (2002).
9. B. T. Rosner, D. W. van der Weide, *Rev. Sci. Instrum.* **73**, 2505 (2002).
10. R. Zoughi, *Microwave Non-Destructive Testing and Evaluation*, Kluwer, The Netherlands, 2000.
11. A. J. Bahr, R. Zoughi, N. Qaddoumi, "Microwave," in *Nondestructive Evaluation*, ed. by P. J. Shull (Marcel Dekker, New York, 2002), p. 645.
12. C. Gao, T. Wei, F. Duewer, Y. Lu and X.-D. Xiang, *Appl. Phys. Lett.* **71**, 1872 (1997).
13. D. W. van der Weide, *Appl. Phys. Lett.* **70**, 677 (1997).
14. D. E. Steinhauer, C. P. Vlahacos, S. Dutta, F. C. Wellstood, S. M. Anlage, *Appl. Phys. Lett.* **71**, 1736 (1997).
15. V. V. Talanov, R. L. Moreland, A. Scherz, A. R. Schwartz, and Y. Liu, *Mater. Res. Soc. Symp. Proc.* **815**, F5.11.1 (2004).
16. S.-C. Lee, C. P. Vlahacos, B. J. Feenstra, A. Schwartz, D. E. Steinhauer, F. C. Wellstood, and S. M. Anlage, *Appl. Phys. Lett.* **77**, 4404 (2000).
17. J. D. Jackson, *Classical Electrodynamics*, 3rd Edition, Wiley, New York, 1999.
18. S. Schelkunoff, *Antennas, Theory and Practice*. Wiley and Sons, Inc., New York, 1952.
19. S. S. Osofsky, S. E. Swarz, *IEEE Trans. Microwave Theory Tech.* **40**, 1701 (1992).
20. D. M. Pozar, *Microwave Engineering*. John Wiley & Sons, Inc., New York, 1998.
21. E. A. Synge, *Phil. Mag. C* **6**, 356 (1928).
22. J. B. Pendry, *Phys. Rev. Lett.* **85**, 3966 (2000).
23. J. B. Pendry, *Phys. Rev. Lett.* **87**, 249704-1 (2001).
24. H. A. Bethe, *Phys. Rev.* **66**, 163 (1944).
25. C. J. Bouwkamp, *Philips Res. Rep.* **5**, 401 (1950).
26. G. A. Massey, *Appl. Optics* **23**, 658 (1984).
27. R. D. Grober, T. Rutherford, T. D. Harris, *Appl. Optics* **35**, 3488 (1996).
28. S. E. Lofland, S. M. Bhagat, H. L. Ju, G. C. Xiong, T. Venkatesan, and R. L. Greene, *Phys. Rev. B* **52**, 15058 (1995).
29. S. E. Lofland, S. M. Bhagat, Q. Q. Shu, M. C. Robson and R. Ramesh, *Appl. Phys. Lett.* **75**, 1947 (1999).
30. E. A. Ash and G. Nicholls, *Nature* **237**, 510 (1972).
31. C. A. Bryant and J. B. Gunn, *Rev. Sci. Instrum.* **36**, 1614 (1965).
32. R. G. Bosio, M. Giroux, and D. Couderc, *J. Microwave Power* **5**, 25 (1970).

33. D. W. Pohl, W. Denk, and M. Lanz, *Appl. Phys. Lett.* **44**, 651 (1984).
34. E. Betzig, M. Isaacson and A. Lewis, *Appl. Phys. Lett.* **51**, 2088 (1987).
35. M. Fee, S. Chu and T. W. Hänsch, *Optics Communications* **69**, 219 (1989).
36. M. Golosovsky and D. Davidov, *Appl. Phys. Lett.* **68**, 1579 (1996).
37. M. Golosovsky, A. Galkin, and D. Davidov, *IEEE Micro. Theor. Tech.* **44**, 1390 (1996).
38. J. Bae, T. Okamoto, T. Fujii, K. Mizuno, T. Nozokido, *Appl. Phys. Lett.* **71**, 3581 (1997).
39. T. Nozokido, R. Iibuchi, J. Bae, K. Mizuno, *Rev. Sci. Instrum.* **76**, 033702 (2005).
40. G. P. Kochanski, *Phys. Rev. Lett.* **62**, 2285 (1989).
41. Y. Manassen, R. J. Hamers, J. E. Demuth, A. J. Castellano *Phys. Rev. Lett.* **62**, 2531 (1989).
42. R. J. Hamers and D. G. Cahill, *Appl. Phys. Lett.* **57**, 2031 (1990).
43. M. Völcker, W. Krieger, H. Walther, *Phys. Rev. Lett.* **66**, 1717 (1991).
44. W. Seifert, E. Gerner, M. Stachel, K. Dransfeld, *Ultramicroscopy* **42**, 379 (1992).
45. U. Ch. Fischer, M. Zapletal, *Ultramicroscopy* **42–44**, 393 (1992).
46. B. Michel, W. Mizutani, R. Schierle, A. Jarosch, W. Knop, H. Benedickter, W. Bächtold, H. Rohrer, *Rev. Sci. Instrum.* **63**, 4080 (1992).
47. W. Mizutani, B. Michel, R. Schierle, H. Wolf, H. Rohrer, *Appl. Phys. Lett.* **63**, 147 (1993).
48. G. Nunes, M. R. Freeman, *Science* **262**, 1029 (1993).
49. S. J. Stranick and P. S. Weiss, *Rev. Sci. Instrum.* **64**, 1232 (1993).
50. S. J. Stranick and P. S. Weiss, *Rev. Sci. Instrum.* **65**, 918 (1994).
51. L. A. Bumm and P. S. Weiss, *Rev. Sci. Instrum.* **66**, 4140 (1995).
52. A. Kramer, F. Keilmann, B. Knoll, R. Guckenberger, *Micron* **27**, 413 (1996).
53. F. Keilmann, D. W. van der Weide, T. Eickelkamp, R. Merz, and D. Stöckle, *Optics Commun.* **129**, 15 (1996).
54. T. Leinhos, O. Rudow, M. Stopka, A. Vollkopf, E. Oesterschulze, *J. Microscopy* **194**, 349 (1999).
55. F. Demming, J. Jersch, S. Klein, K. Dickmann, *J. Microscopy* **201**, 383 (2001).
56. Š. Lányi, M. Hruškovíc, *Rev. Sci. Instrum.* **73**, 2923 (2002).
57. A. Imtiaz and S. M. Anlage, *Ultramicroscopy* **94**, 209 (2003).
58. L. A. Valiente, A. A. P. Gibson, A. D. Haigh, *Electron. Lett.* **40**, 1483 (2004).
59. A. Imtiaz, M. Pollak, S. M. Anlage, J. D. Barry and J. Melngailis, *J. Appl. Phys.* **97**, 044302 (2005).
60. F. Keilmann, *Infrared Phys. Technol.* **36**, 217 (1995).
61. S. J. Stranick, L. A. Bumm, M. M. Kamna, P. S. Weiss, "Linear and nonlinear spectroscopy with the tunable AC scanning tunneling microscope," in *Photons and Local Probes*, ed. by O. Marti and R. Möller (Kluwer, Dordrecht, 1995), p. 221.
62. H. Yokoyama, M. J. Jeffery and T. Inoue, *Jpn. J. Appl. Phys.* **32**, L1845 (1993).
63. H. Yokoyama and M. J. Jeffery, *Colloids and Surfaces A* **93**, 359 (1994).
64. Y. Cho, A. Kirihara and T. Saeki, *Rev. Sci. Instrum.* **67**, 2297 (1996).
65. Y. Cho, S. Kazuta, and K. Matsuura, *Appl. Phys. Lett.* **75**, 2833 (1999).
66. M. Tabib-Azar, Y. Wang, *IEEE Trans. Microwave Theory Tech.* **52**, 971 (2004).
67. H. G. Frey, F. Keilmann, A. Kriele, R. Guckenberger, *Appl. Phys. Lett.* **81**, 5030 (2002).
68. W. Park, J. Kim, K. Lee, *Appl. Phys. Lett.* **79**, 2642 (2001).
69. R. C. Black, F. C. Wellstood, E. Dantsker, A. H. Miklich, D. T. Nemeth, D. Koelle, F. Ludwig, and J. Clarke, *Appl. Phys. Lett.* **66**, 99–101 (1995).

- 240 Steven M. Anlage, Vladimir V. Talanov, and Andrew R. Schwartz
70. R. C. Black, F. C. Wellstood, E. Dantsker, A. H. Miklich, D. Koelle, F. Ludwig, and J. Clarke, *IEEE Trans. Appl. Supercon.* **5**, 2137 (1995).
 71. S.-C. Lee and S. M. Anlage, *Appl. Phys. Lett.* **82**, 1893 (2003).
 72. S.-C. Lee and S. M. Anlage, *IEEE Trans. Applied Supercond.* **13**, 3594 (2003).
 73. S.-C. Lee and S. M. Anlage, *Physica C* **408–410**, 324 (2004).
 74. S.-C. Lee, M. Sullivan, G. R. Ruchti, S. M. Anlage, B. Palmer, B. Maiorov, E. Osquiguil, *Phys. Rev. B* **71**, 014507 (2005).
 75. S.-C. Lee, S.-Y. Lee, and S. M. Anlage *Phys. Rev. B* **72**, 024527 (2005).
 76. C. P. Vlahacos, R. C. Black, S. M. Anlage and F. C. Wellstood, *Appl. Phys. Lett.* **69**, 3272 (1996).
 77. M. Tabib-Azar, N. Shoemaker and S. Harris, *Meas. Sci. Tech.*, **4**, 583 (1993).
 78. A. Tselev, S. M. Anlage, H. Christen, R. L. Moreland, V. V. Talanov, and A. R. Schwartz, *Rev. Sci. Instrum.* **74**, 3167 (2003).
 79. E. Betzig, P. L. Finn, J. S. Weiner, *Appl. Phys. Lett.* **60**, 2484 (1992).
 80. R. Toledo-Crow, P. C. Yang, Y. Chen, M. Vaez-Iravani, *Appl. Phys. Lett.* **60**, 2957 (1992).
 81. K. Karrai, R. D. Grober, *Appl. Phys. Lett.* **66**, 1842 (1995).
 82. M. S. Kim, S. Kim, J. Kim, K. Lee, B. Friedman, J.-T. Kim, J. Lee, *Rev. Sci. Instrum.* **74**, 3675 (2003).
 83. C.-G. Gao, B. Hu, I. Takeuchi, K.-S. Chang, X.-D. Xiang, and G. Wang, *Meas. Sci. Tech.* **16**, 248 (2005).
 84. H. Odagawa and Y. Cho, *Jpn. J. Appl. Phys.* **39**, 5719 (2000).
 85. D. W. van der Weide, P. Neuzil, *J. Vac. Sci. Technol. B* **14**, 4144 (1996).
 86. *Scanning Tunneling Microscopy*, ed. by J. A. Stroscio and W. J. Kaiser, Academic Press, New York (1993).
 87. R. Wiesendanger, *Scanning Probe Microscopy and Spectroscopy: Methods and Applications*, Cambridge (1994).
 88. B. Knoll, F. Keilmann, A. Kramer, R. Guckenberger, *Appl. Phys. Lett.* **70**, 2667 (1997).
 89. M. Tabib-Azar, D.-P. Su, A. Pohar, S. R. LeClair, G. Ponchak, *Rev. Sci. Instrum.* **70**, 1725 (1999).
 90. F. Duewer, C. Gao, I. Takeuchi, X.-D. Xiang, *Appl. Phys. Lett.* **74**, 2696 (1999).
 91. F. Duewer, C. Gao, I. Takeuchi, X.-D. Xiang, *Rev. Sci. Instrum.* **71**, 2414 (2000).
 92. B. Knoll and F. Keilmann, *Appl. Phys. Lett.* **77**, 980 (2000).
 93. D. E. Steinhauer, C. P. Vlahacos, S. K. Dutta, B. J. Feenstra, F. C. Wellstood, S. M. Anlage, *Appl. Phys. Lett.* **72**, 861 (1998).
 94. A. S. Thanawalla, S. K. Dutta, C. P. Vlahacos, D. E. Steinhauer, B. J. Feenstra, S. M. Anlage, and F. C. Wellstood, *Appl. Phys. Lett.* **73**, 2491 (1998).
 95. A.N. Reznik, N.V. Yurasova, *Tech. Phys.*, **49**, 485 (2004).
 96. S. Ramo, J. R. Whinnery, T. V. Duzer, *Fields and Waves in Communication Electronics*. John Wiley & Sons, Inc., New York, 1994.
 97. Z.-Y. Shen, *High-Temperature Superconductive Microwave Circuits*. Artech House, Inc., Boston, 1994.
 98. R. E. Matick, *Transmission Lines for Digital and Communication Networks*, IEEE Press, New York, 1995.
 99. M. Hein, *High-Temperature-Superconductor Thin Films at Microwave Frequencies*, Springer Tracts in Modern Physics, Vol. 155, Springer-Verlag, 1999.
 100. S.-C. Lee, Ph.D. thesis, University of Maryland, 2004.

I.7. Principles of Near-Field Microwave Microscopy 241

101. C. P. Vlahacos, D. E. Steinhauer, S. K. Dutta, B. J. Feenstra, S. M. Anlage, and F. C. Wellstood, *Appl. Phys. Lett.*, **72**, 1778 (1998).
102. D. E. Steinhauer, Ph.D. Thesis, University of Maryland (2000).
103. V. V. Talanov, L. V. Mercaldo, S. M. Anlage, and J. H. Claassen, *Rev. Sci. Instrum.* **71**, 2136 (2000).
104. T. Tran, D. R. Oliver, D. J. Thomson, and G. E. Bridges, *Rev. Sci. Instrum.* **72**, 2618 (2001).
105. C. Gao, and X.-D. Xiang, *Rev. Sci. Instrum.* **69**, 3846 (1998).
106. M. Tabib-Azar, D. Akinwande, G. Ponchak, and S. R. LeClair, *Rev. Sci. Instrum.* **70**, 3381 (1999).
107. M. Tabib-Azar, D. Akinwande, *Rev. Sci. Instrum.*, **71**, 1460 (2000).
108. M. Tabib-Azar, T. Zhang, and S. R. LeClair, *IEEE Trans. Instrum. Meas.* **51**, 1126 (2002).
109. *Waveguide handbook*, ed. N. Marcuvitz. McGraw-Hill Book Co., Inc., New York, 1951.
110. D. E. Steinhauer, C. P. Vlahacos, C. Canedy, A. Stanishevski, J. Melngailis, R. Ramesh, F. C. Wellstood, and S. M. Anlage, *Appl. Phys. Lett.* **75**, 3180 (1999).
111. X.-D. Xiang, C. Gao, P. G. Schultz, T. Wei, US Patent # 6,532,806 (2003).
112. R. W. P. King, M. Owens, T. T. Wu, *Lateral Electromagnetic Waves*, Springer-Verlag, New York, 1992.
113. A. Imtiaz and S. M. Anlage, ~~in preparation (2006)~~.
114. V. V. Talanov, A. Scherz, R. L. Moreland, A. R. Schwartz, ~~submitted to~~ *Appl. Phys. Lett.*, ~~available at <http://arxiv.org/abs/cond-mat/0511475>~~.
115. M. Tabib-Azar, P. S. Pathak, G. Ponchak, and S. LeClair, *Rev. Sci. Instrum.* **70**, 2783 (1999).
116. J. Kim, M. Kim, H. Kim, D. Song, K. Lee, B. Friedman, *Appl. Phys. Lett.* **83**, 1026 (2003).
117. M. Kim, J. Kim, H. Kim, S. Kim, J. Yang, H. Yoo, S. Kim, K. Lee, B. Friedman, *Rev. Sci. Instrum.* **75**, 684 (2004).
118. V. S. Zuev and A. V. Frantsesson, *J. Commun. Tech. and Electronics* **43**, 1021 (1998).
119. Š. Lányi, M. Hruškovíc, *J. Phys. D* **36**, 598 (2003).
120. J. H. Lee, S. Hyun, K. Char, *Rev. Sci. Instrum.* **72**, 1425 (2001).
121. S. M. Anlage, B. J. Feenstra, D. E. Steinhauer, US Patent # 6,376,836 (2002).
122. R. Hillenbrand, F. Keilmann, *Phys. Rev. Lett.* **85**, 3029 (2000).
123. E. Tanabe and W. T. Joines, *IEEE Trans. Instrum. Meas.* **IM-25**, 222 (1976).
124. M. A. Stuchly and S. S. Stuchly, *IEEE Trans. Instrum. and Meas.* **IM-29**, 176 (1980).
125. Y. Lu, T. Wei, F. Duerwer, Y. Lu, N. Ming, P. G. Schultz and X.-D. Xiang, *Science* **276**, 2004 (1997).
126. B. J. Feenstra, C. P. Vlahacos, A. S. Thanawalla, D. E. Steinhauer, S. K. Dutta, F. C. Wellstood and S. M. Anlage, *IEEE MTT-S Int. Microwave Symp. Digest*, p. 965 (1998).
127. C. P. Vlahacos, D. E. Steinhauer, S. M. Anlage, F. C. Wellstood, S. K. Dutta, J. B. Feenstra, *The Americas Microscopy and Analysis*, January, 13 (2000).
128. Y. G. Wang, M. E. Reeves, F. J. Rachford, *Appl. Phys. Lett.* **76**, 3295 (2000).
129. Y. Cho, S. Kazuta, K. Ohara, H. Odagawa, *Jpn. J. Appl. Phys.* **39**, 3086 (2000).
130. D. E. Steinhauer, C. P. Vlahacos, F. C. Wellstood, S. M. Anlage, C. Canedy, R. Ramesh, A. Stanishevsky, and J. Melngailis, *Rev. Sci. Instrum.* **71**, 2751 (2000).
131. D. E. Steinhauer and S. M. Anlage, *J. Appl. Phys.* **89**, 2314 (2001).

- 242 Steven M. Anlage, Vladimir V. Talanov, and Andrew R. Schwartz
132. Y. G. Wang, M. E. Reeves, W. J. Kim, J. S. Horwitz, and F. J. Rachford, *Appl. Phys. Lett.* **78**, 3872 (2001).
 133. Y. J. Feng, L. Y. Wu, T. Jiang, L. Liu, L. Kang, S. Z. Yang, P. H. Wu, *Supercond. Sci. Technol.* **15**, 390 (2002).
 134. Y.-C. Chen, H.-F. Cheng, G. Wang, X.-D. Xiang, C.-M. Lei, I.-N. Lin, *Jpn. J. Appl. Phys.* **41**, 7214 (2002).
 135. Z. Wang, M. A. Kelly, Z.-X. Shen, G. Wang, X.-D. Xiang, J. T. Wetzel, *J. Appl. Phys.* **92**, 808 (2002).
 136. C. Gao, B. Hu, P. Zhang, M. Huang, W. Liu, I. Takeuchi, *Appl. Phys. Lett.* **84**, 4647 (2004).
 137. A. Tselev and S. M. Anlage, in preparation, 2006.
 138. H. Chang, C. Gao, I. Takeuchi, Y. Yoo, J. Wang, P. G. Schultz, X.-D. Xiang, R. P. Sharma, M. Downes, and T. Venkatesan, *Appl. Phys. Lett.* **72**, 2185 (1998).
 139. H. Chang, I. Takeuchi, X.-D. Xiang, *Appl. Phys. Lett.* **74**, 1165 (1999).
 140. Y. K. Yoo, F. Duewer, T. Fukumura, H. Yang, D. Yi, S. Liu, H. Chang, T. Hasegawa, M. Kawasaki, H. Koinuma, X.-D. Xiang, *Phys. Rev. B* **63**, 224421 (2001).
 141. H. Chang, K.-M. Yu, Y. Dong, X.-D. Xiang, *Appl. Phys. Lett.* **81**, 2062 (2002).
 142. N. Okazaki, S. Okazaki, H. Higuma, S. Miyashita, Y. Cho, J. Nishimaru, T. Fukumura, M. Kawasaki, M. Murakami, Y. Yamamoto, Y. Matsumoto, H. Koinuma, T. Hasegawa, *Applied Surface Science* **223**, 196 (2004).
 143. H.-W. Cheng, X.-J. Zhang, S.-T. Zhang, Y. Feng, Y.-F. Chen, Z.-G. Liu, G.-X. Cheng, *Appl. Phys. Lett.* **85**, 2319 (2004).
 144. X.-D. Xiang, *Appl. Surf. Sci.* **223**, 54 (2004).
 145. I. Takeuchi, R.B. van Dover, and H. Koinuma, *Mater. Res. Soc. Bull.* **27**, 301 (2002).
 146. H. Koinuma, I. Takeuchi, *Nature Materials* **3**, 429 (2004).
 147. Y. Cho and K. Ohara, *Appl. Phys. Lett.* **79**, 3842 (2001).
 148. C. Hubert, J. Levy, *Rev. Sci. Instrum.* **70**, 3684 (1999).
 149. C. Hubert, J. Levy, E. J. Cukauskas, S. W. Kirchoefer, *Phys. Rev. Lett.* **85**, 1998 (2000).
 150. S. Hyun, J. H. Lee, S. S. Kim, K. Char, S. J. Park, J. Sok, E. H. Lee, *Appl. Phys. Lett.* **77**, 3084 (2000).
 151. H. Odagawa and Y. Cho, *Appl. Phys. Lett.* **80**, 2159 (2002).
 152. M. J. Werner and R. J. King, *MRS Proc.* **430**, 67 (1996).
 153. Y. S. Xu and R. G. Bosisio, *IEE Proc. H* **139**, 500 (1992).
 154. R. J. Gutman and J. M. Borrego, *IEEE MTT Digest*, 281 (1987).
 155. H. Bhimnathwala and J. M. Borrego, *J. Vac. Sci. Technol. B* **12**, 395 (1994).
 156. T. Nozokido, J. Bae, K. Mizuno, *IEEE Trans. Microwave Theory Tech.* **49**, 491 (2001).
 157. Y. Huang, C. C. Williams, J. Slinkman, *Appl. Phys. Lett.* **66**, 344 (1995).
 158. M. Tabib-Azar, D. Akinwande, G. Ponchak, S. R. LeClair, *Rev. Sci. Instrum.* **70**, 3083 (1999).
 159. C. C. Watson, W. K. Chan, *Appl. Phys. Lett.* **78**, 129 (2001).
 160. M. Tabib-Azar, R. Ciocan, G. Ponchak, and S. R. LeClair, *Rev. Sci. Instrum.* **70**, 3387 (1999).
 161. J.-P. Bourgoin, M. B. Johnson, B. Michel, *Appl. Phys. Lett.* **65**, 2045 (1994).
 162. B. Knoll and F. Keilmann, *Optics Commun.* **182**, 321 (2000).
 163. A comprehensive discussion of the VideoDisc technology may be found in a collection of articles published in *RCA Rev.* **39** (1978).
 164. J. R. Matey and J. Blanc, *J. Appl. Phys.* **57**, 1437 (1985).

165. C. D. Bugg and P. J. King, *J. Phys. E* **21**, 147 (1988).
166. H. P. Kleinknecht, J. R. Sandercock, H. Meier, *Scanning Microscopy* **2**, 1839 (1988).
167. Š. Lányi, J. Török, P. Řehůřek, *Rev. Sci. Instrum.* **65**, 2258 (1994).
168. Š. Lányi, J. Török, P. Řehůřek, *J. Vac. Sci. Technol. B* **14**, 892 (1996).
169. A. F. Lann, M. Golosovsky, D. Davidov, and A. Frenkel, *Appl. Phys. Lett.* **73**, 2832 (1998).
170. A. Kim, J. Kim, S. Hyun, S. S. Kim, T. Kim, K. Char, *Rev. Sci. Instrum.* **74**, 3164 (2003).
171. S. M. Anlage, C. P. Vlahacos, D. E. Steinhauer, S. K. Dutta, B. J. Feenstra, A. Thanawalla, and F. C. Wellstood, *Particle Accelerators* **61**, 321./57 (1998). Also available at <http://www.arXiv.org/abs/cond-mat/9808195>.
172. S. M. Anlage, D. E. Steinhauer, C. P. Vlahacos, B. J. Feenstra, A. S. Thanawalla, W. Hu, S. K. Dutta, and F. C. Wellstood, *IEEE Trans. Appl. Supercond.* **9**, 4127 (1999).
173. Y. J. Feng, L. Liu, Z. L. Fu, L. Y. Wu, Q. G. Liu, L. X. You, L. Kang, S. Z. Yang, P. H. Wu, S. Z. Wang, *IEEE Trans. Applied Supercond.* **11**, 123 (2001).
174. F. Sakran, M. Golosovsky, H. Goldberger, D. Davidov, A. Frenkel, *Appl. Phys. Lett.* **78**, 1634 (2001).
175. J. Kim, K. Lee, B. Friedman, D. Cha, *Appl. Phys. Lett.* **83**, 1032 (2003).
176. Z. Wang, M. A. Kelly, Z.-X. Shen, L. Shao, W.-K. Chu, H. Edwards, *Appl. Phys. Lett.* **86**, 153118 (2005).
177. M. Abu-Teir, F. Sakran, M. Golosovsky, D. Davidov, A. Frenkel, *Appl. Phys. Lett.* **80**, 1776 (2002).
178. A. F. Lann, M. Golosovsky, D. Davidov, A. Frenkel, *Appl. Phys. Lett.* **75**, 603 (1999).
179. S. Hyun, J. H. Cho, A. Kim, J. Kim, T. Kim, and K. Char, *Appl. Phys. Lett.* **80**, 1574 (2002).
180. B. A. Auld, and D. K. Winslow, "Microwave Eddy-Current Experiments with Ferromagnetic Resonance Probes," in *Eddy-Current Characterization of Materials and Structures* (ASTM Special Technical Publication 722, Philadelphia, 1981), p. 348.
181. F. Sakran, A. Copty, M. Golosovsky, and D. Davidov, P. Monod, *Appl. Phys. Lett.* **84**, 4499 (2004).
182. Z. Zhang, P. C. Hammel and P. Wigen, *Appl. Phys. Lett.* **68**, 2005 (1996).
183. Z. Zhang, P. C. Hammel, M. Midzor, M. L. Roukes, and J. R. Childress, *Appl. Phys. Lett.* **73**, 2036 (1998).
184. G. R. Eaton and S. S. Eaton, *Bull. Mag. Res.* **10**, 22 (1987).
185. M. Ikeya and T. Miki, *Jap. J. Appl. Phys.* **26**, L929 (1987).
186. M. Ikeya, M. Furusawa, and M. Kasuyai, *Scanning Microscopy* **4**, 245 (1990).
187. M. Ikeya, "ESR Microscopy," in *New Applications of Electron Spin Resonance* (World Scientific, Singapore, 1993), p. 427.
188. M. Hirai, C. Yamanaka, M. Ikeya, *Appl. Radiation and Isotopes* **44**, 385 (1993).
189. K. Wago, D. Botkin, C. S. Yannoni, and D. Rugar, *Appl. Phys. Lett.* **72**, 2757 (1998).
190. F. Sakran, A. Copty, M. Golosovsky, N. Bontemps, D. Davidov, A. Frenkel, *Appl. Phys. Lett.* **82**, 1479 (2003).
191. Y. Manassen, *Adv. Mater.* **6**, 401 (1994).
192. C. Durkan and M. E. Welland, *Appl. Phys. Lett.* **80**, 458 (2002).
193. I. Takeuchi, T. Wei, F. Duewer, Y. K. Yoo, X.-D. Xiang, V. Talyansky, S. P. Pai, G. J. Chen, and T. Venkatesan, *Appl. Phys. Lett.* **71**, 2026 (1997).
194. A. F. Lann, M. Abu-Teir, M. Golosovsky, D. Davidov, A. Goldgirsch, and V. Berlin, *Appl. Phys. Lett.* **75**, 1766 (1999).

- 244 Steven M. Anlage, Vladimir V. Talanov, and Andrew R. Schwartz
195. S. M. Anlage, C. P. Vlahacos, S. Dutta, and F. C. Wellstood, *IEEE Trans. Appl. Supercond.* **7**, 3686 (1997).
196. A. F. Lann, M. Abu-Teir, M. Golosovsky, D. Davidov, S. Djordjevic, N. Bontemps, and L. F. Cohen, *Rev. Sci. Instrum.* **70**, 4348 (1999).
197. W. Hu, B. J. Feenstra, A. S. Thanawalla, F. C. Wellstood, and S. M. Anlage *Appl. Phys. Lett.* **75**, 2824 (1999).
198. S. M. Anlage, W. Hu, C. P. Vlahacos, D. Steinhauer, B. J. Feenstra, S. K. Dutta, A. Thanawalla, and F. C. Wellstood, *J. Supercond.* **12**, 353 (1999).
199. E. C. Burdette, F. L. Cain, and J. Seals, *IEEE Trans. Microwave Theory Tech.* **MTT-28**, 414 (1980).
200. T. W. Athey, M. A. Stuchly and S. S. Stuchly, *IEEE Trans. Microwave Theory and Tech.* **MTT-30**, 82 (1982).
201. M. A. Stuchly, T. W. Athey, G. M. Samaras and G. E. Taylor, *IEEE Trans. Microwave Theory and Tech.* **MTT-30**, 87 (1982).
202. M. Tabib-Azar, J. L. Katz, and S. R. LeClair, *IEEE Trans. Instrum. Meas.* **48**, 1111 (1999).
203. S. M. Anlage, A. S. Thanawalla, A. P. Zhuravel', W. Hu, C. P. Vlahacos, D. E. Steinhauer, S. K. Dutta, and F. C. Wellstood, "Near-Field Scanning Microwave Microscopy of Superconducting Materials and Devices," in *Advances in Superconductivity XI*, ed. by N. Koshizuka and S. Tajima, (Springer-Verlag, Tokyo, 1999), pp. 1079.
204. A. S. Thanawalla, W. Hu, D. E. Steinhauer, S. K. Dutta, B. J. Feenstra, S. M. Anlage, F. C. Wellstood, and R. B. Hammond, *IEEE Trans. Appl. Supercond.* **9**, 3042 (1999).
205. S. Hong, J. Kim, W. Park, K. Lee, *Appl. Phys. Lett.* **80**, 524 (2002).
206. K. S. Chang, M. Aronova, O. Famodu, I. Takeuchi, S. E. Lofland, J. Hatrick-Simpers, H. Chang, *Appl. Phys. Lett.* **79**, 4411 (2001).
207. L. B. Felsen, N. Marcuvitz, *Radiation and Scattering of Waves*, IEEE Press, Piscataway, NJ, 1994.
208. C. Gao, F. Duewer, and X.-D. Xiang, *Appl. Phys. Lett.* **75**, 3005 (1999).
209. H. Zheng, J. Wang, S. E. Lofland, Z. Ma, L. Mohaddes-Ardabili, T. Zhao, L. Salamanca-Riba, S. R. Shinde, S. B. Ogale, F. Bai, D. Viehland, Y. Jia, D. G. Schlom, M. Wuttig, A. Roytburd, R. Ramesh, *Science* **303**, 661 (2004).
210. E. Saitoh, H. Miyajima, T. Yamaoka, G. Tatara, *Nature* **432**, 203 (2004).
211. Y. Cho, K. Fujimoto, Y. Hiranaga, Y. Wagatsuma, A. Onoe, K. Terabe, K. Kitamura, *Appl. Phys. Lett.* **81**, 4401 (2002).
212. K. Fujimoto and Y. Cho, *Jpn. J. Appl. Phys.* **43**, 2818 (2004).
213. A. V. Balatsky, Y. Manassen, R. Salem, *Phys. Rev. B* **66**, 195416 (2002).
214. C. Durkan, *Contemp. Phys.* **45**, 1 (2004).
215. S. I. Kiselev, J. C. Sankey, I. N. Krivorotov, N. C. Emley, R. J. Schoelkopf, R. A. Buhrman, D. C. Ralph, *Nature* **425**, 380 (2003).
216. F. Kreupl, A. P. Graham, G. S. Duesberg, W. Steinhögl, M. Liebau, E. Unger and W. Hönlein, *Microelec. Eng.* **64**, 399 (2002).
217. P. J. Burke, *IEEE Trans. Nanotech.* **1**, 129 (2002).
218. A. Coptly, M. Golosovsky, D. Davidov, A. Frenkel, *IEEE Trans. Microwave Th. Tech.* **52**, 1957 (2004).
219. R. A. Shelby, D. R. Smith, and S. Schultz, *Science* **292**, 77 (2001).
220. V. G. Veselago, *Usp. Fiz. Nauk* **92**, 517 (1967) {English translation: *Sov. Phys. Usp.* **10**, 509 (1968)}.
221. A. A. Houck, J. B. Brock, I. L. Chuang, *Phys. Rev. Lett.* **90**, 137401 (2003).

I.7. Principles of Near-Field Microwave Microscopy 245

222. D. R. Smith, D. Schurig, M. Rosenbluth, S. Schultz, S. A. Ramakrishna, J. B. Pendry, *Appl Phys. Lett.* **82**, 1506 (2003).
223. N. Fang, H. Lee, C. Sun, X. Zhang, *Science* **308**, 534 (2005).
224. J. B. Pendry, A. J. Holden, D. J. Robbins, W. J. Stewart, *J. Phys. Condens. Matter* **10**, 4785 (1998).
225. T. W. Ebbesen, H. J. Lezec, H. F. Ghaemi, T. Thio, P. A. Wolff, *Nature* **391**, 667 (1998).